Correlating surface crystal orientation and gas kinetics in perovskite-oxide electrodes

Ran Gao[1*], Abel Fernandez[1*], Tanmoy Chakraborty[2], Aileen Luo[1], David Pesquera[1,3], Sujit Das[1], Gabriel Velarde[1], Vincent Thoréton[4], John Kilner[4,5], Tatsumi Ishihara[4], Slavomír Nemšák[6], Ethan J. Crumlin[6], Elif Ertekin[7], Lane W. Martin[1,8,#]

[1] Department of Materials Science and Engineering, University of California, Berkeley, Berkeley, CA 94720, USA

[2] Beckman Institute for Advanced Science and Technology, University of Illinois at Urbana−Champaign, Urbana, Illinois 61801, USA

[3] Catalan Institute of Nanoscience and Nanotechnology, Campus UAB, Bellaterra, 08193 Barcelona, Spain

[4] WPI International Institute for Carbon-Neutral Energy Research (WPI-I2CNER), Kyushu University, Fukuoka 81-0395, Japan

[5] Department of Materials, Imperial College London, London SW72AZ, UK

[6] Advanced Light Source, Lawrence Berkeley National Laboratory, Berkeley, CA 94720, USA

[7] Department of Mechanical Science and Engineering, University of Illinois, Urbana-Champaign, Urbana, IL 61801, USA

[8] Materials Sciences Division, Lawrence Berkeley National Laboratory, Berkeley, CA 94720, USA

* These authors contributed equally to this work.

Corresponding author: lwmartin@berkeley.edu

Abstract

Solid-gas interactions at electrode surfaces determine the efficiency of solid-oxide fuel cells and electrolyzers. Here, the correlation between surface-gas kinetics and the crystal orientation of perovskite electrodes is studied in the model system $La_{0.8}Sr_{0.2}Co_{0.2}Fe_{0.8}O_3$. The gas-exchange kinetics are characterized by synthesizing epitaxial half-cell geometries where three single-variant surfaces are produced [*i.e.*, $La_{0.8}Sr_{0.2}Co_{0.2}Fe_{0.8}O_3/La_{0.9}Sr_{0.1}Ga_{0.95}Mg_{0.05}O_{3-\delta}/SrRuO_3/ SrTiO_3$ (001), (110), and (111)]. Electrochemical impedance spectroscopy and electrical conductivity relaxation measurements reveal a strong surface-orientation dependency of the gas-exchange kinetics, wherein (111)-oriented surfaces exhibit an activity >3-times higher as compared to (001)-oriented surfaces. Oxygen partial pressure (p_{O_2}) dependent electrochemical impedance spectroscopy studies reveal that while the three surfaces have different gas-exchange kinetics, the reaction mechanisms and rate-limiting steps are the same (*i.e.*, charge-transfer to the diatomic oxygen species). First-principles calculations suggest that the formation energy of vacancies and adsorption at the various surfaces is different and influenced by the surface polarity. Finally, synchrotron-based, ambient-pressure X-ray spectroscopies reveal distinct electronic changes and surface chemistry among the different surface orientations. Taken together, thin-film epitaxy provides an efficient approach to control and understand the electrode reactivity ultimately demonstrating that the (111)-surface exhibits a high density of active surface sites which leads to higher activity.

Introduction

Strong interactions with gas molecules at the solid-gas interface have made perovskite ABO_3 oxides promising electrode candidates for intermediate-temperature solid-oxide fuel cells and

electrolyzers[1–3]. Nevertheless, the rate of oxygen electrocatalysis at the electrode surface remains one of the major factors that limits device efficiency. Extensive work has been performed to understand the surface-gas kinetics of perovskite electrodes and its correlation with specific properties such that better electrodes can be designed. Compositional screening has identified important electronic factors, such as the occupancy of the *B*-site cation e_g orbitals[4,5] or the relative position of the oxygen 2*p* band center[6], both of which can act as descriptors for predicting high electrochemical activity. As such, controlling the electronic structure of perovskite electrodes *via* chemical-doping has been the prevailing route to optimize gas-exchange kinetics.

Beyond chemistry control, advances in thin-film synthesis now enable researchers to study surface reactions on an oriented single-crystal facet where extrinsic factors of bulk ceramics can be eliminated, and new methods of structural control can be realized. For instance, epitaxial strain has been found to influence both the surface-gas kinetics and ionic conductivity of perovskites, where the *B*-O-*B* bond strength and angle have been identified as important factors affecting both oxygen exchange and mobility[7–11]. Other studies have focused on the relative importance of both surface-termination and sub-surface chemistry of (001)-oriented perovskite surfaces in dictating electrochemical reaction rates[12–15]. Perovskite electrodes with different exposed crystallographic orientations have also been reported to have different electrochemical reaction rates[16–18]. Attempts to study surface-orientation effects on the gas-exchange kinetics of perovskite electrodes have been accomplished by growing single-layer-perovskite electrodes on perovskite substrates, typically employing techniques such as isotope-tracer diffusion, electrical-conductivity relaxation and solution-based electrochemical cells[16–22]. Generally, such studies point to faster kinetics on (111) surfaces and slow kinetics on (001) surfaces, whereas (110) surfaces have provided somewhat contradictory results[16–18,22]. Nevertheless, there remains a need for detailed mechanistic

insights on orientation dependence. Here, we focus on the role of surface orientation in dictating the gas-reaction kinetics of perovskite electrodes.

Examining the impact of surface orientations on gas-exchange kinetics requires the construction of well-defined electrode surfaces and a reliable probe of the gas-exchange kinetics. Previous AC-impedance studies on electrochemical cells composed of yttria-stabilized zirconia (YSZ) or other fluorite-based electrolytes with perovskite micro-electrodes have provided mechanistic insight about the surface-gas reactions[23–25]. The structural mismatch, however, between the electrode and electrolyte results in the creation of polycrystalline electrodes and/or the formation of defective heterointerfaces. Such defects can complicate the interpretation of results and limit control of the perovskite-electrode structure (*e.g.*, varying the surface orientations, and/or altering the strain). Here, we bridge the gap between half-cell-based electrochemical-impedance spectroscopy studies and epitaxial thin-film studies by developing an all-perovskite, epitaxial half-cell heterostructure to examine the orientation-dependent gas-exchange kinetics. Both approaches assure the level of synthetic control typically associated with high-quality epitaxial thin films for further quantitative surface analysis.

In particular, we utilize epitaxial thin-films of $La_{0.8}Sr_{0.2}Co_{0.2}Fe_{0.8}O_{3-\delta}$ (LSCF) on $SrTiO_3$ substrates as a model system to probe electrochemical differences between different crystallographic surfaces. Preliminary studies based on electrical-conductivity-relaxation establish that (111) surfaces have the fastest reaction rates, while (001) surfaces are slowest, and (110) surfaces have an intermediate reaction rate. We proceed to develop all-perovskite epitaxial thin-film half-cells of the form 30 nm LSCF (working electrode)/150 nm $La_{0.9}Sr_{0.1}Ga_{0.95}Mg_{0.05}O_{3-\delta}$ (LSGM, electrolyte)/20 nm $SrRuO_3$ (counter electrode)/$SrTiO_3$ (001), (110), and (111) with the film orientation being set by the substrate. Electrical measurements of the epitaxial half-cells are

achieved via microfabrication of the top working electrode (LSCF) into well-defined circular electrodes and applying small AC voltages between the working and counter electrodes. Electrochemical-impedance spectroscopy reveals that, at 350°C, the (111) surfaces have a gas-kinetic-rate constant more than 3- and 2-times higher than that of the (001) and (110) surfaces, respectively. Oxygen-partial pressure (p_{O_2}) dependent electrochemical-impedance spectroscopy of the half-cells suggests that the rate-limiting step of the surface reaction is the charge-transfer process to adsorbed oxygen adatoms (for $p_{O_2} > 1$ Torr) and the absorbance of oxygen molecules (for $p_{O_2} < 1$ Torr) for all three surface orientations. This indicates that while similar surface reactions occur on all three orientations, the (111) surfaces contain more active reaction sites to account for the differences. Density-functional theory (DFT) calculations reveal that the different surfaces have different stability with respect to the process of vacancy formation and oxygen adsorption, which stabilizes different surface chemistries. This is corroborated by ambient-pressure X-ray photoelectron (AP-XPS) and absorption spectroscopy (AP-XAS), which reveal the presence of different surface chemistries, with the (111) surfaces containing more oxygen vacancies, less surface-strontium segregation, and more near-surface *B*-site cations. This study reveals the importance of surface versus bulk chemistry and the role that vacancy-formation energy plays in stabilizing surface chemistries that promote oxygen exchange.

Experimental

Synthesis of epitaxial thin-films and half-cell structures

The thin-film heterostructures were synthesized *via* pulsed-laser deposition using a KrF excimer laser (248 nm; LPX 305, Coherent, Inc.) on $SrTiO_3$ (001), (110), and (111) substrates (Crystec, GmBH). The $SrRuO_3$ bottom electrode layers were deposited from a ceramic target (Praxair) of

the same chemistry deposited at a heater temperature of 700°C in a dynamic p_{O_2} of 100 mTorr with a laser fluence of 1.3 J/cm^2 and a repetition rate of 15 Hz. Following the growth of the $SrRuO_3$, the LSGM layers were deposited from a ceramic target of the same chemistry ($La_{0.9}Sr_{0.1}Ga_{0.95}Mg_{0.05}O_3$) at a heater temperature of 800°C in a dynamic p_{O_2} of 40 mTorr with a laser fluence of 1.7 J/cm^2 and repetition rate of 5 Hz. Following the growth of the LSGM, the LSCF films were grown from a ceramic target (Praxair) of the same chemistry ($La_{0.8}Sr_{0.2}Co_{0.2}Fe_{0.8}O_{3-\delta}$) at a heater temperature of 700°C in a dynamic p_{O_2} of 150 mTorr with a laser fluence of 1.6 J/cm^2 and repetition rate of 5 Hz. Following deposition, the films and heterostructures were cooled in a static p_{O_2} of 700 Torr at 10°C/min. For the single-layer LSCF films, the growth conditions were maintained as noted above, but growth was completed directly on the $SrTiO_3$ (001), (110), and (111) substrates.

Film crystal structure, surface, and surface stoichiometry characterization

X-ray studies were conducted with a high-resolution X-ray diffractometer (X'pert Pro3, PANalytical). θ-2θ line scans were used to probe the out-of-plane orientation of both single-layer films and tri-layer heterostructures from 10-70°. Two-dimensional reciprocal space mapping (RSM) studies were carried out to verify the epitaxy and strain state of the heterostructures. For the (001), (110), and (111) surfaces, the 103-, 221-, and 312-diffraction conditions were chosen, respectively, to obtain in-plane structural information for each heterostructure type. Surface topography was studied using an atomic force microscope (MFP-3D, Asylum Research). The outermost surface chemistry of the LSCF films was examined by low-energy ion scattering (LEIS) using a QTAC 100 (IONTOF). Prior to measurement the sample was cleaned in a preparation chamber in flowing oxygen for 40 min. before loading into the measurement chamber. The spectra were recorded with a 6 keV neon beam (1 nA) over a 1 mm^2 area in static conditions.

Electrical-conductivity-relaxation measurements

Electrical-conductivity-relaxation measurements were performed on 40-nm-thick, single-layer LSCF films with four platinum contacts deposited at the corners. The platinum contacts were then gold-wire bonded to a CERDIP chip carrier, which was subsequently loaded in the measurement setup. The measurement setup includes a home-built, tube-furnace-based measurement setup (Supplementary Fig. 1). An Al_2O_3 tube was sealed using KF flanges on both ends, with one end connected to a mechanical pump and the other with a customized KF-type flange through which we accomplished sample connection, gas inlet, and temperature monitoring. An alumina bar is mounted on the flange to hold the CERDIP chip carrier, and four silver wires with thermal shields were used to connect the chip carrier with external BNC ports via electrical feedthroughs. A Keithley 2400 current-voltage source was used (driving at 10 mV for current measurements) to monitor the electrical resistance change of the sample after a step change in pressure. The step change in p_{O_2} is controlled by a sudden open and close of the outlet pumping port, while the pressure was monitored simultaneously.

Fabrication of half-cell structures

Half-cell fabrication was carried out via a series of pulsed-laser deposition and photolithography steps (Supplementary Fig. 2). Initially, a bilayer consisting of the $SrRuO_3$ counter-electrode layer and the LSGM electrolyte were synthesized *in situ* via pulsed-laser deposition. A photolithography step is used to define the circular area that will define the LSCF electrodes. The patterned sample is then returned to the pulsed-laser deposition chamber, and a room-temperature deposition of 80 nm of MgO followed by 30 nm of ZnO is deposited using a laser fluence of 2.0 J/cm^2 at a repetition rate of 15 Hz and a pressure of 5 mTorr in both cases. Following ZnO/MgO deposition, the photoresist is removed with acetone and isopropanol rinses, leaving a hard mask to define the

LSCF electrodes[26], with the LSGM surface exposed. The LSGM surface is then plasma-cleaned for 60 sec. and immediately returned to the pulsed-laser deposition chamber. LSCF top electrodes are then deposited using the same conditions as the single-layer films. Following deposition, a continuous LSCF layer covers the entire structure. Liftoff of the underlying ZnO layer with a NaOH etch selectively dissolves the ZnO and removes excess LSCF that is not defined by the circular areas of the hardmask leaving the MgO insulating layer, and exposed circular electrodes of LSCF. A final photolithography step is performed to define the platinum pads which are used for wire-bonded electrical connection to the LSCF electrode. Liftoff of the excess photoresist with acetone leaves well-defined platinum pads that contact the edge of the LSCF electrode, completing the half-cell heterostructure.

Electrochemical-impedance-spectroscopy studies

Electrochemical-impedance-spectroscopy measurements were carried out in the same home-built, tube-furnace-based measurement setup (Supplementary Fig. 1). A PARSTAT 3000 potentiostat was used to perform the electrochemical-impedance-spectroscopic measurements from 0.5 Hz to 500 kHz using a 10 mV excitation. For temperature control, an additional thermocouple was placed immediately adjacent to the sample holder to measure temperature near the sample surface. During the measurement, the temperature is monitored via the internal thermocouple mounted in proximity to the chip carrier and the PID setting of the heater was tuned to assure stable temperatures for this sample geometry. p_{O_2} was controlled by fixing the inlet flow of oxygen (flow rate at 4 sccm), while the outlet pumping speed was adjusted by changing the opening of the outlet pumping port to achieve target pressure. Using this setup, pressure control from 80 mTorr to 760 Torr is achievable. Before measuring, the samples were allowed to equilibrate at each pressure and temperature for 20 minutes.

Density-functional-theory calculations

All total-energy calculations were performed using plane-wave density functional theory (DFT) as implemented in the Vienna Ab Initio Simulation Package (VASP)[27–29]. The Perdew-Burke-Ernzerhof (PBE) approximation to the exchange-correlation functional and projector augmented wave[30] pseudopotentials were used. We include the Hubbard *U* (GGA+U)[31,32] term to improve the description of the localized cobalt and iron 3*d*, with U = 5 eV for both. For the plane-wave basis a cutoff energy of 520 eV was used. Brillouin zone sampling was sufficient in all cases to converge total energies to within 0.01 eV per slab. All calculations were spin-polarized and initialized with a ferromagnetic configuration of cobalt and iron atoms, which was allowed to relax. The atomic coordinates and the volume of all the surfaces were fully relaxed during the simulations until the Hellmann-Feynman forces on each atom were below 0.01 eV/A. We have used graphical visualization package VESTA[33] for all the surface models.

The DFT slab composition was $La_{0.75}Sr_{0.25}Co_{0.25}Fe_{0.75}O_3$ which is close to the experimentally synthesized sample. We simulated (La,Sr)O-, O_2-, and (La,Sr)O_3-terminated surfaces for (001)-, (110)-, and (111)-surface orientations, respectively. For all surface models we used symmetric slabs to avoid surface-dipole moments, with a vacuum region of 15 Å. The *A*- and *B*-site cation sublattices were occupied by lanthanum/strontium and iron/cobalt in an ordered manner for simplicity. For the (001) surface, there were a total of seven layers, four *A*O and three *B*O_2 layers, containing 136 atoms in the supercell. For the (110) surface, there were a total of nine layers, four *AB*O and five O_2 layers, containing 88 atoms in the supercell. For the (111) surface, there were a total of 13 layers, seven *A*O_3 and six *B* layers, containing 136 atoms in the supercell. We used a 2x2x1 gamma-point *k*-mesh for the (001) and (111) surfaces and a 2x3x1 *k*-mesh for

the (110) surface. The slab energies were converged to within 5 meV per formula unit with respect to the *k*-points and energy cutoff.

The oxygen vacancy formation energy $E[V_O]$ and the energy of the surface with the oxygen molecule adsorbed at the vacancy site $E\left[{O_2}^{ads}\right]$ are referenced to the as-cleaved surface and, respectively, given by:

$$E[V_O] = E[\text{surface} + V_O] - E[\text{surface}] + \frac{1}{2}\mu_{O_2}$$

$$E\left[{O_2}^{ads}\right] = E[\text{surface} + V_O + O_2] - E[\text{surface}] - \frac{1}{2}\mu_{O_2}$$

where $E[\text{surface}]$, $E[\text{surface} + V_O]$, $E[\text{surface} + V_O + O_2]$ are the total energies of the as-cleaved slabs, slabs with an oxygen vacancy present, and slabs with an oxygen molecule adsorbed into the vacant site, respectively. The quantity $\frac{1}{2}\mu_{O_2}$ is the chemical potential of oxygen, obtained here for standard conditions; note that we used the corrected value for the DFT-computed oxygen molecule energy owing to the fact that PBE is known to overbind the molecule.

Ambient-pressure X-ray absorption and photoelectron spectroscopy

AP-XAS and AP-XPS measurements were carried out on 20-nm-thick LSCF single-layer films at Beamline 9.3.2 of the Advanced Light Source at Lawrence Berkeley National Laboratory[34]. Following alignment, samples were cleaned by heating to 350°C in 10 mTorr of oxygen while observing the carbon 1*s* peak shrink. After cleaning, the chamber was again pumped to 10^{-8} Torr and measurements were performed with increasing p_{O_2}. A photon energy of 670 eV was used for all AP-XPS measurements. Each measurement sequence took approximately 3 hours to obtain high-resolution oxygen 1*s*, strontium 3*d*, lanthanum 4*d*, and cobalt/iron 3*p* spectra in addition to the oxygen *K*-, cobalt *L*-, and iron *L*-edge absorption spectra. All XPS spectra were calibrated to the lanthanum 4*d* 5/2 excitation at 104.5 eV. Curve-fitting of the obtained XPS spectra was

performed using the CasaXPS software with a symmetric line shape produced from a Gaussian/Lorentzian product function, after subtracting a Shirley-type background. For strontium 3*d* fitting of the spin-orbit split doublet, a fixed branching ratio of 3:2 and energy separation of 1.8 eV was used. For lanthanum 4*d* fitting, a branching ratio of 3:2 and energy separation of 2.8 eV was used. Analysis of the surface stoichiometry was performed by scaling the integrated area of the peak of interest with its respective photoionization cross-section. The cobalt and iron *L*-edge XAS spectra were normalized to the peak intensity of the white line, without any pre-edge subtraction. The oxygen *K* edge was normalized by scaling the difference in background intensity before (~525 eV) and after (~548 eV) the main features in order to consistently normalize without the molecular oxygen adsorption at ~530 eV influencing normalization.

Results & Discussion

LSCF films

We began by synthesizing single-layer LSCF films on $SrTiO_3$ (001), (110), and (111) substrates via pulsed-laser deposition. X-ray diffraction line scans reveal single-phase, high-quality, epitaxial films wherein the growth orientation is set by the substrate (Fig. 1a). The LSCF composition used in this study is closely lattice-matched to the $SrTiO_3$ substrate, and only the Laue thickness fringes are visible in the line scan[35]. The films have smooth surfaces with similar root-mean-squared roughness as revealed by atomic force microscopy (Supplementary Fig. 3). LEIS was used to study of the surface termination and revealed that, for all heterostructures, the outermost layer is *A*-site cation terminated (Supplementary Fig. 4). The only nuance being that the (111) surfaces show evidence of a low concentration of exposed *B*-site cations. This is consistent with previous studies which suggest that the outermost layer is primarily *A*-site cations, and *B*-site cations are present

only in sub-surface layers[36]. Thus, the (001) and (111) surfaces should be (La,Sr)O- and (La,Sr)O_3-terminated, respectively. For the (110) surfaces, although the expected termination is (La,Sr)(Co,Fe)O, no detectable *B*-site cations are present, indicating there has been significant *A*-site segregation. This is confirmed by the strontium-to-lanthanum peak intensity ratios extracted from the LEIS of 1.44, 0.87, and 1.20 for the (001), (110), and (111) surfaces, respectively; all of which are larger than the ideal ratio of 0.25 (Supplementary Fig. 4, inset). This suggests that despite identical growth conditions and strain states, the different crystallographic surfaces stabilize different surface chemistries, which may deviate from the expected bulk stoichiometry.

As a first probe of the electrochemical activity of these surfaces, we performed electrical-conductivity-relaxation experiments on the three surface variants. Previous studies have shown different strontium-segregation rates for different perovskite surfaces, and that high levels of segregation can override the intrinsic differences in reactivity of the different crystal surfaces. As such, we performed electrochemical measurements at 350°C to slow the strontium-segregation kinetics. We measured the relaxation of normalized resistance from the LSCF layers following a step-change in pressure from 380 Torr to 200 Torr (Fig. 1b) resulting in the fastest response for (111)-oriented films, with the (001)-oriented films demonstrating the slowest response. The extracted k^{chem} rate constants[10,37] (Fig. 1c), show that (111) surfaces are nearly 5 times as reactive as (110)- and (001) surfaces. The observation of fast kinetics on (111)-oriented surfaces is in agreement with studies on related perovskite systems[16,17] and the magnitude of k^{chem} is comparable to studies on LSC-based electrodes measured at similar temperatures[16,17,38]. With the electrochemical trend established, we turn to half-cell-based measurements to further explore the origin of this orientation dependence.

Epitaxial perovskite half-cells

In order to probe mechanistic differences governing the oxygen exchange on the different surface variants, we developed an epitaxial, all-perovskite, half-cell device for use in electrochemical impedance spectroscopy experiments. The heterostructures are grown via pulsed-laser deposition and have the form 30 nm LSCF/150 nm LSGM/20 nm $SrRuO_3$/$SrTiO_3$ (001), (110), and (111). X-ray diffraction line scans reveal that all heterostructures are composed of single-phase, high-quality, epitaxially grown layers wherein the growth orientation is set by the substrate (Fig. 2a-c). RSM studies suggest that all layers are epitaxially aligned and coherently strained (Supplementary Fig. 5).

The half-cell structures, shown schematically (Fig. 2d,e), were subsequently fabricated into real devices (Fig. 2f) to enable studies of the electrochemical response. As illustrated, the LSCF-working electrodes (diameter $200\ \mu m$) are connected to platinum contacts by an arm that just touches the edge of the electrode; negligibly impacting the working area. The platinum contacts are insulated from the rest of the cell by an amorphous, insulating MgO layer. To analyze the impedance response, a lumped-element equivalent circuit is employed, consistent with work elsewhere (Fig. 2d)[39,40]. The top part of the circuit is given by parallel elements including a surface resistance R_s and a constant-phase element Q_s, which together describe the surface-reaction process at the electrode-gas interface. Using circular electrodes with 200 µm diameter makes the electrochemical R_s (> 10 kΩ) much larger than the ionic-transport impedance across the 150 nm electrolyte with same cross-section (<10 Ω based on the ionic conductivity for single-crystalline LSGM[7,41] and LSCF[42]); this allows us to lump the ionic transmission line into a simple resistor given by the ionic-transport impedance R_{ion}. The bottom part of the circuit is the charge-transfer impedance at the LSGM-$SrRuO_3$ interface which is described by a parallel resistance R_{ct} and a constant-phase element Q_{ct}. Owing to the fact that the $SrRuO_3$ is metallic and the electrolyte is

thin, under small electrical perturbations, the ionic charges at the LSGM-$SrRuO_3$ interface are expected to be mainly compensated by the stoichiometric change of the LSGM electrolyte. Qualitatively, we assume that such stoichiometry change in the thin LSGM electrolyte is limited by diffusion at dilute concentration, and that the charge-transfer process is expected to show up at much higher frequencies in the impedance spectra compared to the surface-reaction process owing to small R_{ion}. To further validate this assumption and to confirm that the geometry is surface-reaction-limited, we have performed a set of additional experiments on the half-cells including working-electrode deactivation, electrode-area dependence, and electrolyte-thickness dependence studies, which all suggest that the major potential drop happens at the LSCF-gas interface (Supplementary Materials, Supplementary Fig. 6). Thus, in this geometry, operation of the half-cell is surface-reaction-limited, providing a platform to isolate and study the active electrode-surface reaction.

Electrochemical testing of surface variants

Electrochemical-impedance spectroscopy of the half-cells with different surface orientations was performed at 350°C in both air and dry oxygen. Representative spectra for the three half-cell orientations (Fig. 3a) reveal that all half-cell variants show a single, well-defined semicircle. The high-frequency intercepts (~ 1 $k\Omega$) likely arise from contributions of both ionic-transport (R_{ion}) and charge-transfer (R_{ct}) impedance. The low-frequency endpoints reflect the rate of the surface-gas reaction. Fitting the spectra to the equivalent circuit yields R_s which can be further converted into a surface-gas reaction rate constant $k^q = \frac{kT}{4e^2(R_s \cdot A)c_o}$, where A is the electrode area and c_o is the concentration of oxygen species calculated based on reported values[47]. The rate constants (in air) reveal that the (111) surfaces have reaction rates >3- and 2-times higher than that of the (001)

and (110) surfaces, respectively (Fig. 3b). In dry oxygen, the trend holds the same for the three orientations except for an overall higher reaction rate due to a richer oxygen concentration. The error bars are determined by measuring multiple devices each on two different sets of half-cell heterostructures; the small deviation indicates good consistency and repeatability[48]. The results from impedance spectroscopy exhibit the same trend and similar relative magnitudes of k^q compared to k^{chem} extracted from electrical-conductivity-relaxation measurements. These two measurements point to the same performance trend: (111) surfaces have gas-reaction-rate constants many times higher than the (001) and (110) surfaces.

Probing the rate-limiting step

Although the surface-gas reaction can be decomposed into several elementary steps (*e.g.*, adsorption of oxygen molecules, reduction of adsorbed species, ion incorporation, etc.), it is assumed that at one step will be rate-limiting and dictate the p_{O_2}-dependence of the reaction[43–45] The resulting surface-reaction impedance will be related to p_{O_2} according to: $1/R_s \propto (p_{O_2})^m$, where m depends on the nature of the rate-limiting step. To understand the reaction mechanisms, p_{O_2}-dependent electrochemical-impedance spectroscopy (from 0.08-760 Torr) was performed (Fig. 3c-e and Supplementary Fig. 7). All three surface variants were found to exhibit essentially the same p_{O_2} dependence, differing only in magnitude of R_s. At low pressures ($p_{O_2} < 1$ Torr), $m \approx 1$ corresponding to a reaction that involves diatomic oxygen. In this case, the reaction may be limited simply by the surface coverage of adsorbed oxygen molecules (*i.e.*, $O_{2,\,gas} \rightarrow O_{2,\,ad}$) or by charge-transfer to the adsorbed oxygen (*i.e.*, $O_{2,ad} \rightarrow O_{2,ad}^{-} + h^{+}$ or $O_{2,ad}^{-} \rightarrow O_{2,ad}^{2-} + h^{+}$)[43]. At high pressures ($p_{O_2} > 1$ Torr), $m \approx 0.25$ and likely corresponds with a charge-transfer-limited reaction. Here the species involved can be either dissociated, adsorbed oxygen atoms (O_{ad}) or

diatomic oxygen in one of three charge states: neutral $O_{2,ad}$, superoxo $O_{2,ad}^{-}$, or peroxo $O_{2,ad}^{2-}$. In the case of O_{ad}-reduction, this implies a change in the rate-limiting-step from adsorption to charge transfer as p_{O_2} increases, whereas in the latter case, one rate-limiting, charge-transfer step (*i.e.*, $O_{2,ad}^{-} \rightarrow O_{2,ad}^{2-} + h^{+}$) dominates the entire pressure regime, and the crossover in *m* is driven by a change in the surface coverage and resulting electrostatic interactions of charged-surface species[49]. With all surfaces demonstrating the same crossover, however, it appears there is no mechanistic difference that can explain the differences in reaction rate between the surfaces. Thus, we turn our focus to the details of the adsorption and charge-transfer process that determine the reaction rate.

Exploring rate-limiting energetics from first principles

To explore possible surface structural and electronic differences that could drive the observed electrochemical differences, we used DFT calculations to understand the driving forces for oxygen exchange on each surface[52,53]. We began by simulating the defect-free surfaces for each of the orientations, using *A*-site terminations enriched with 50% strontium to reflect the LEIS measurements. For (001) and (111) surfaces, this entails *A*O- and AO_3-termination, respectively, while for (110) surfaces, we examined both defect-free *AB*O- and O_2-terminated surfaces under the assumption that the two terminations are convertible and coexisting by oxygen adsorption/desorption. We calculated the energies of these surfaces following introduction of a surface-oxygen vacancy and subsequently an adsorbed-oxygen molecule and performing these calculations over sites that have either subsurface cobalt or iron allowed for comparison of the relative energies for oxygen exchange for the different *B*-site species.

The (001) (Fig. 4a), (110) (Fig. 4b), and (111) (Fig. 4c) surfaces were found to exhibit markedly different energy profiles for the hypothesized pathway. Focusing first on vacancy formation, the calculations reveal a sizable increase in energy (2-2.5 eV) when an oxygen vacancy is introduced to the (100) surface (Fig. 4a)[46]. On the other hand, vacancy formation on (111) surfaces results in a decrease in energy (Fig. 4c). This suggests that (111) surfaces are prone to spontaneous vacancy formation, while (100) surfaces limit vacancy formation. For (110) surfaces, the relationship is less clear (Fig. 4b). In the case of *AB*O-termination, vacancy formation results in an increase in energy (4.5 eV) even greater than that for the (100) surface, while vacancy formation on the O_2-terminated surface results in a significant decrease in energy (0.72-0.9 eV), similar to the (111) surface. In other words, oxygen vacancies on (110) surfaces are unstable in the *AB*O plane, but are stable above the cations in the O_2 plane.

These trends are consistent with what would be expected from electrostatic considerations of surface polarity. For the (001) surface, an *A*O-termination with a stoichiometric La:Sr ratio of 4:1 leaves the defect-free surface with a net charge of +0.8 per formula unit. Vacancy formation on this surface would further increase the surface charge, indicating it is unfavorable to form vacancies. Replacing lanthanum with strontium (*i.e.*, strontium segregation) would reduce the net charge thereby electrostatically stabilizing the surface. The stoichiometric *AB*O-terminated (110) surfaces are similarly positively charged, and vacancy formation would worsen the electrostatic stability. Again, strontium segregation serves to reduce the surface charge and stabilize the surface. Applying the same treatment to the AO_3-terminated (111) surfaces, the net charge of the surface is -3.2 per formula unit, and thus formation of positively charged oxygen vacancies serves to stabilize the surface polarity, likely explaining the favorability to form such vacancies observed in DFT. Thus, for both the (001) and (110) surfaces, surface charge hinders vacancy formation, and may

provide an additional driving force for strontium segregation, in addition to elastic and chemical driving forces[47].

Turning to the adsorption of molecular oxygen, the calculations reveal that adsorption at an oxygen-vacancy site results in a lowering of the surface energy in all cases, supporting studies that identify vacancy sites as the primary active site[48]. Additionally, we note that the bond-length of the adsorbed-oxygen molecule (~1.35 Å) is increased relative to that of molecular oxygen (1.23 Å), indicative of an activated, superoxo $O_{2,ad}^{-}$ as the stable adsorbed species; lending support to the reaction $O_{2,ad}^{-} \rightarrow O_{2,ad}^{2-} + h^{+}$as the rate-limiting step[43,48]. Interestingly, when the energies of the different subsurface cations are weighted by their relative concentration, the (100) and (111) surfaces have similar energy reductions upon adsorption of oxygen molecules (~1.1 eV) suggesting that the stabilization of vacancy sites on (111) surfaces is the main driving force for the increased electrochemical performance. The O_2-terminated (110) surface has the most favorable energy of adsorption (~1.8 eV) while the *AB*O-terminated (110) surface has the least favorable adsorption energy (~0.7 eV). Thus, the (110) surface presents a case where the different terminations work in opposition, and the electrochemical results may reflect the competition between the (un)favorable terminations. These results, in conjunction with the absence of surface *B*-site cations in the LEIS data, merit a deeper study of possible surface reconstructions at these polar surfaces, and particularly on (110) surfaces.

Surface electronic structure in ambient conditions

Considering the DFT results, we aimed to directly probe the electronic structure associated with each surface orientation. To do this we performed AP-XAS and AP-XPS which allow for the measurement of elemental-specific spectra at high temperatures and in ambient gas environments[34].

For each surface variant, the cobalt and iron *L*-edges and oxygen *K*-edges were probed at 350°C in oxygen pressures from 10^{-8} to 0.9 Torr to understand how the electronic structure is influenced by the interaction with molecular oxygen (Fig. 5a-c). While the XAS results are qualitatively similar across the different surface orientations (Supplementary Figs. S9-11), their pressure dependence provides insight into the interaction of these surfaces with oxygen molecules. At low p_{O_2}, both the iron (Fig. 5a) and cobalt (Fig. 5b) *L*-edge spectra suggest that the cations have predominantly 3+ valence[49–51]. As oxygen is introduced the iron *L*-edge shows no change, whereas the cobalt *L*-edge broadens to higher photon energies, indicating an increase towards 4+ valence. This agrees with studies in bulk ceramics, where changing oxygen stoichiometry results in larger changes to the cobalt valence[52]. It has been shown that the electronic structure of iron changes from $3d^5$ to $3d^5\underline{\mathrm{L}}$, where $\underline{\mathrm{L}}$ indicates a ligand hole, with increasing oxidation[49]. As such, changing the oxygen content of the lattice results in hole doping of primarily oxygen 2*p* character, and can be observed in measurements of the oxygen *K* edge (Fig. 5c). We observe two broad features at 535 eV and 542 eV, corresponding to lanthanum/strontium 3*d* – oxygen 2*p* hybridized states, and cobalt/iron 3*p* – oxygen 2*p* hybridized states, respectively; however, the most significant changes are observed around a sharp peak at 530 eV, corresponding to excitations involving cobalt/iron 3*d* – oxygen 2*p* hybridized states. At low p_{O_2}, this peak is relatively sharp, and is attributed to excitation into unoccupied $t_{2g}\downarrow$ states. As the pressure is increased, an increase in intensity at 528 eV is observed, suggesting the depopulation of some $e_g\uparrow$ states[53,54] (*i.e.*, hole-doping of the oxygen 2*p* states as electrons are transferred to adsorbed oxygen to form the superoxo $O_{2,ad}^-$ state). This pre-peak area provides a quantitative marker of oxygen adsorption (*i.e.*, $[h^+]$), and comparison of the rate of pre-peak change for different surface orientations reveals a strong preference for hole doping on (110) surfaces as compared to (001) and (111) surfaces (Fig. 5d). The similarity in

driving force for oxygen adsorption provided by DFT for the (001) (-1.1 eV) and (111) (-1.37 eV) surfaces is manifested in the similar rate of pre-peak area increase extracted from XAS. The larger slope for the (110) surfaces may point to adsorption in the O_2-plane rather than the *AB*O-plane considering the larger driving force for oxygen-molecule adsorption (-1.87 eV). Thus, the distinct bonding environments of each surface orientation give rise to distinct electronic interactions with oxygen.

Understanding surface structure and chemistry

The understanding gleaned from the LEIS, DFT, and XAS analysis naturally raises the question if different surface chemistries drive the observed electrochemical differences? We also measured the oxygen 1*s*, cobalt/iron 3*p*, strontium 3*d*, lanthanum 4*d*, and valence-band photoelectron excitations with a probing depth of ~1 nm using AP-XPS. We initially focus on the strontium 3*d* excitation, owing to the well-known deleterious effect of strontium segregation on catalytic reactivity[55,56]. For all three orientations, we observe the complex peak shapes typically found for strontium 3*d* peaks which are decomposed into a low- and high-binding-energy doublet which we attribute to "lattice-like" and "surface-like" strontium species, respectively (Fig. 6a-c)[57]. A more detailed discussion of the assignment of these peaks is presented in the Supplementary Materials. The "surface-like" excitation is observed to increase over the duration of the measurement at 350°C, suggesting active strontium segregation (Fig. 6d); however, the (111) surface maintains the lowest "surface-like" contribution throughout. This supports the notion that the (111) surfaces have an electrostatic driving force originating from the surface polarity that limits strontium segregation compared to the other surfaces, in agreement with previous studies[58]. This strontium-enriched surface can be confirmed without invoking the "surface-like" assignment by comparing

the total ratio of strontium to *A*-site species in the near-surface region (Fig. 6e). We see that while all surface orientations have a higher strontium concentration than the bulk stoichiometry, the (111) surface has the lowest overall concentration of near-surface strontium.

Both the AP-XPS and LEIS point to significant deviations of the surface chemistry from the bulk stoichiometry. As such, we aimed to understand how these deviations impact the near-surface *B*-site chemistry, which is expected to impact the available reaction sites. We quantify the *B*-site chemistry using the integrated peak areas from the core-level excitations for all cations, scaled appropriately by their respective photoionization cross-sections (Supplementary Materials)[59]. The (111) surfaces have the largest fraction of near-surface *B*-site cations (Fig. 6f). The trends in the fraction of *B*-site cations track closely with the trends in electrochemical response, whereas solely looking at the segregated strontium does not. It is interesting to note that, despite similar surface terminations among the three surfaces, a high degree of near-surface or subsurface *B*-site cations still enhances the catalytic reactivity[14,15]. Ultimately, these differences in surface chemistry explain the lack of mechanistic differences among the three surfaces. With a charge-transfer-limited reaction, surface vacancies and near-surface *B*-site cations are needed for the formation of $O_{2,ad}^{-}$ and subsequent reduction. Stabilizing high oxygen-vacancy concentration and a "large" number of *B*-site cations near the surface and limiting the electrostatic driving force for strontium segregation that quenches these sites results in faster reaction rates for the (111) surfaces.

Conclusions

We have demonstrated epitaxial all-perovskite half-cells that serve as a platform to study the electrochemical response of perovskite cathodes. Such epitaxial control allows for study of the electrochemical response of the different surfaces, revealing large differences in electrochemical

activity. While (001), (110), and (111) surfaces exhibit the same rate-limiting step for oxygen exchange, combined DFT and spectroscopic analyses reveal that the local bonding environment at the surface stabilizes distinct (non-bulk-like) surface chemistries. These results highlight the importance of understanding the possible surface reconstructions, and how deviations from bulk stoichiometry at surfaces may hinder otherwise favorable reaction kinetics. Fast reaction kinetics are found at (111) surfaces that exhibit a balance of important factors such as vacancy concentration, favorable adsorption energy, low strontium segregation, and high *B*-site availability. Whereas many studies have pursued performance optimization by tuning the bulk stoichiometry, new avenues for engineering can be envisioned whereby the materials chemistry is engineered to effect favorable surface chemistries and therefore higher catalytic activities.

Conflicts of interest

There are no conflicts to declare.

Acknowledgements

R.G., A.F., A.L., T.C., E.E., and L.W.M. acknowledge the support of the National Science Foundation under Grant OISE-1545907. D.P. acknowledges funding from the European Union's Horizon 2020 research and innovation programme under the Marie Skłodowska-Curie grant agreement No. 797123. G.V. acknowledges the support of the National Science Foundation under Grant DMR-1708615. V.T. and T.I. acknowledge financial support from a Grant-in-Aid for Specially Promoted Research No.16H06293) from MEXT, Japan and through the Japan Society for the Promotion of Science and the Solid Oxide Interfaces for Faster Ion Transport JSPS Core-

to-Core Program (Advanced Research Networks). J.K. acknowledge the support by World Premier International Research Center Initiative (WPI), Ministry of Education, Culture, Sports, Science, and Technology of Japan (MEXT), Japan, Solid Oxide Interfaces for Faster Ion Transport (SOIFIT) JSPS/EPSRC (EP/P026478/1) Core-to-Core Program (Advanced Research Networks). This research used resources of the Advanced Light Source, which is a DOE Office of Science User Facility under contract no. DE-AC02-05CH11231.

Figures and Captions

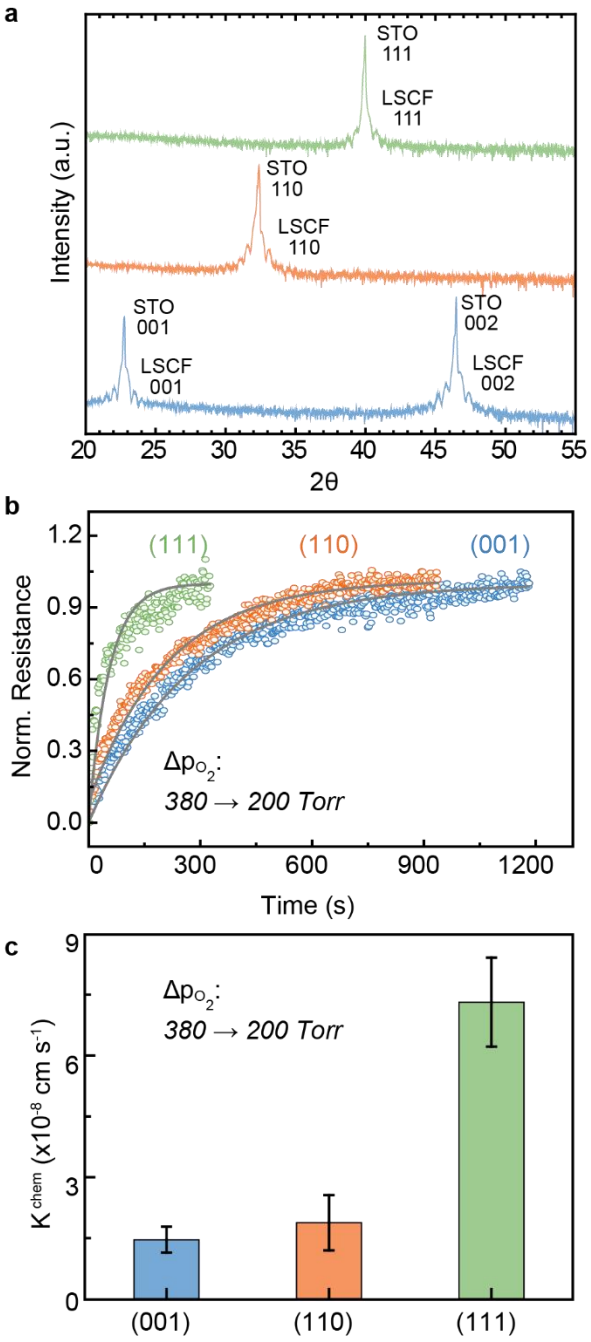

Fig. 1 | Electrical conductivity relaxation on epitaxial $La_{0.8}Sr_{0.2}Co_{0.2}Fe_{0.8}O_3$ thin films. X-ray diffraction line-scans reveal high-quality epitaxial $La_{0.8}Sr_{0.2}Co_{0.2}Fe_{0.8}O_3$ (LSCF) on (001)-, (110)-, and (111)-oriented $SrTiO_3$ substrates. (**b**) Electrical-resistivity-relaxation measurements on single-layer LSCF films demonstrate fast kinetics on (111) surfaces. (**d**) Rate constants extracted from fitting of relaxation measurements indicates the same performance trend as half-cell studies, with the fastest exchange happening on (111) surfaces.

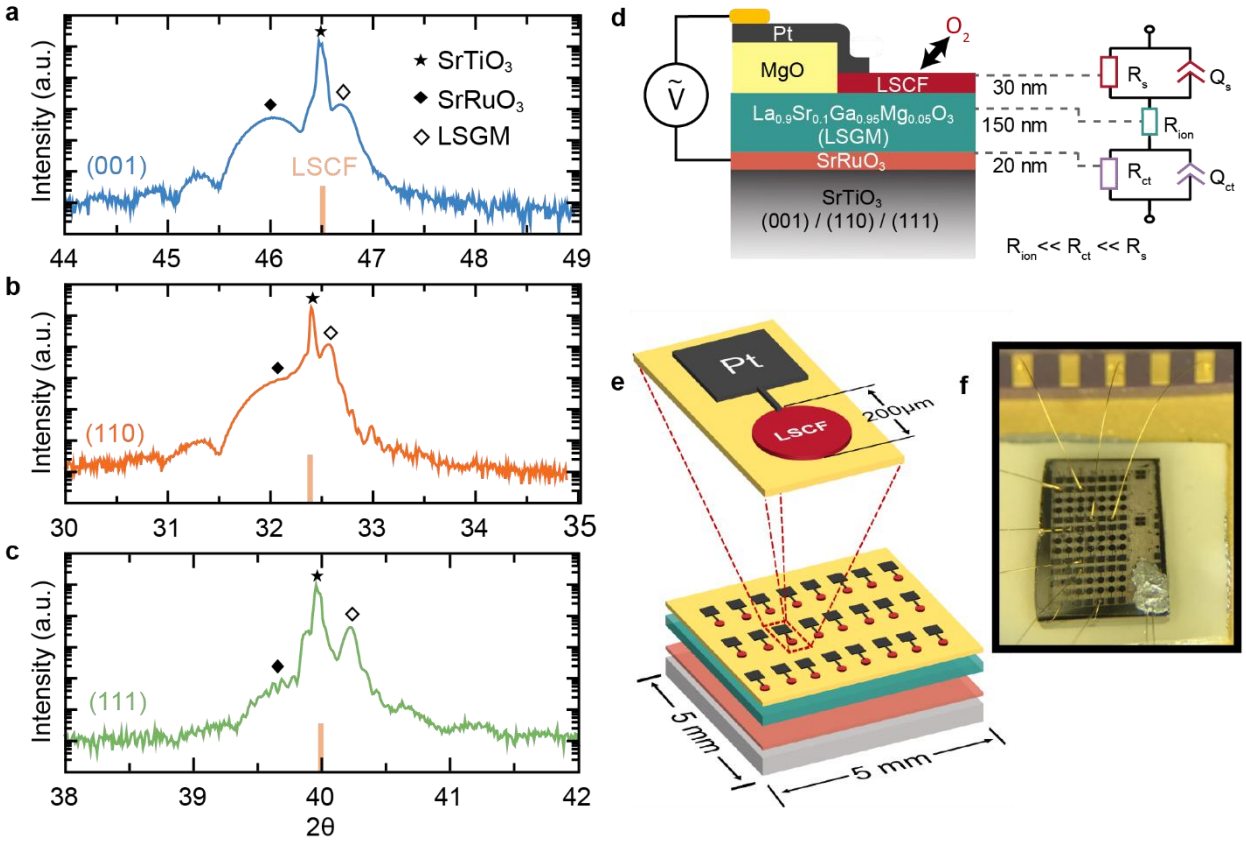

Fig. 2 | Epitaxial all-perovskite half-cells with controlled surface orientation. X-ray diffraction line-scans reveal high-quality epitaxial $La_{0.8}Sr_{0.2}Co_{0.2}Fe_{0.8}O_3$ (LSCF)/$La_{0.9}Sr_{0.1}Ga_{0.95}Mg_{0.05}O_3$ (LSGM)/$SrRuO_3$ trilayer structures grown on (**a**) (001)-, (**b**) (110)-, and (**c**) (111)-oriented $SrTiO_3$ substrates. (**d**) A cross-section of the heterostructure and the corresponding equivalent circuit used for analysis of the half-cell. (**e**) Microfabrication provides a large number of devices to be patterned on a 5 x 5 mm substrate, allowing for statistical analysis of many devices.

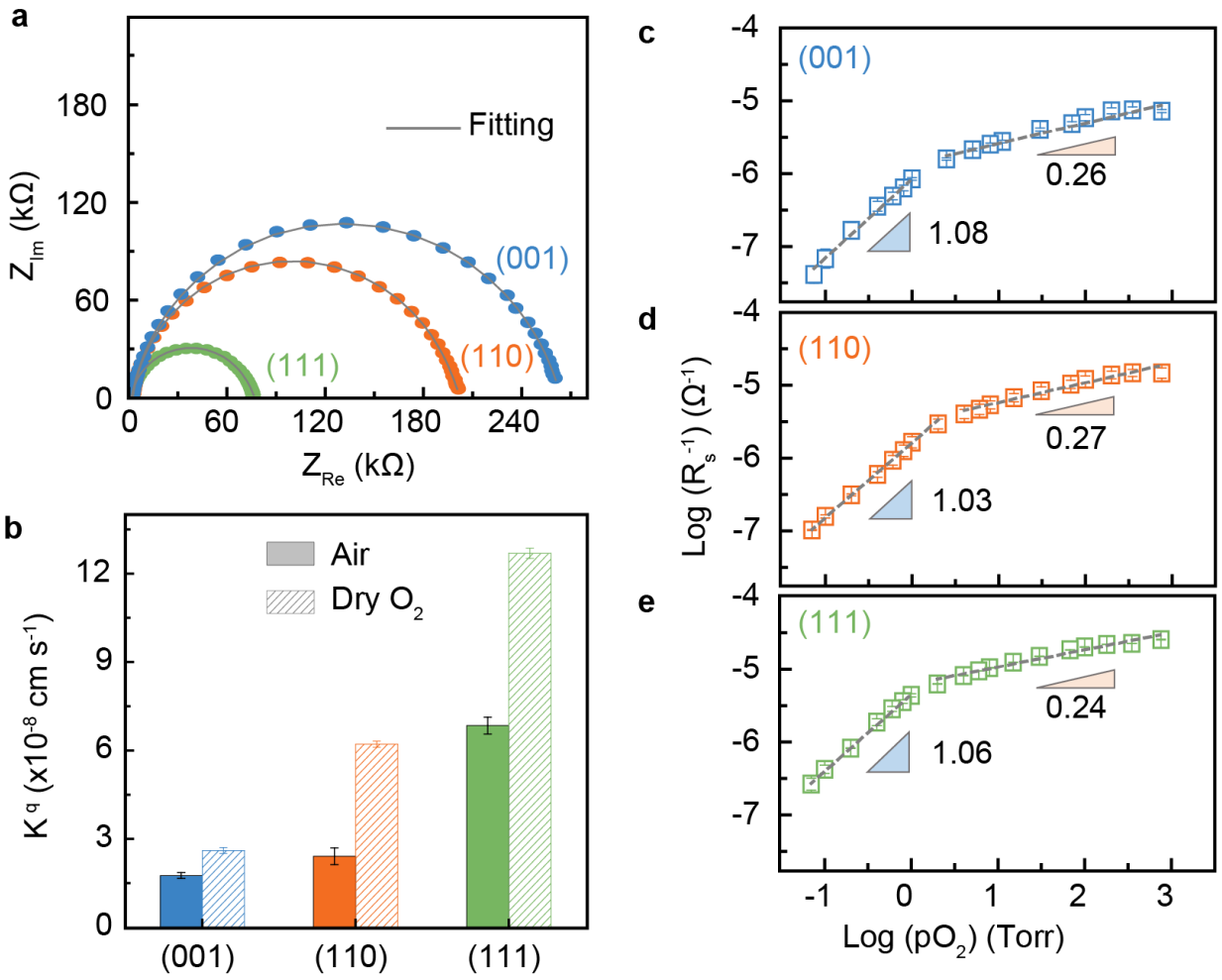

Fig. 3 | Electrochemical measurements of LSCF cathodes with different surface orientations. (**a**) Representative Nyquist plots from electrochemical-impedance-spectroscopy studies measure on the different surface variants in a dry O_2 environment. (**b**) Rate constants calculated from the extracted R_s values illustrate the large difference in rate constant

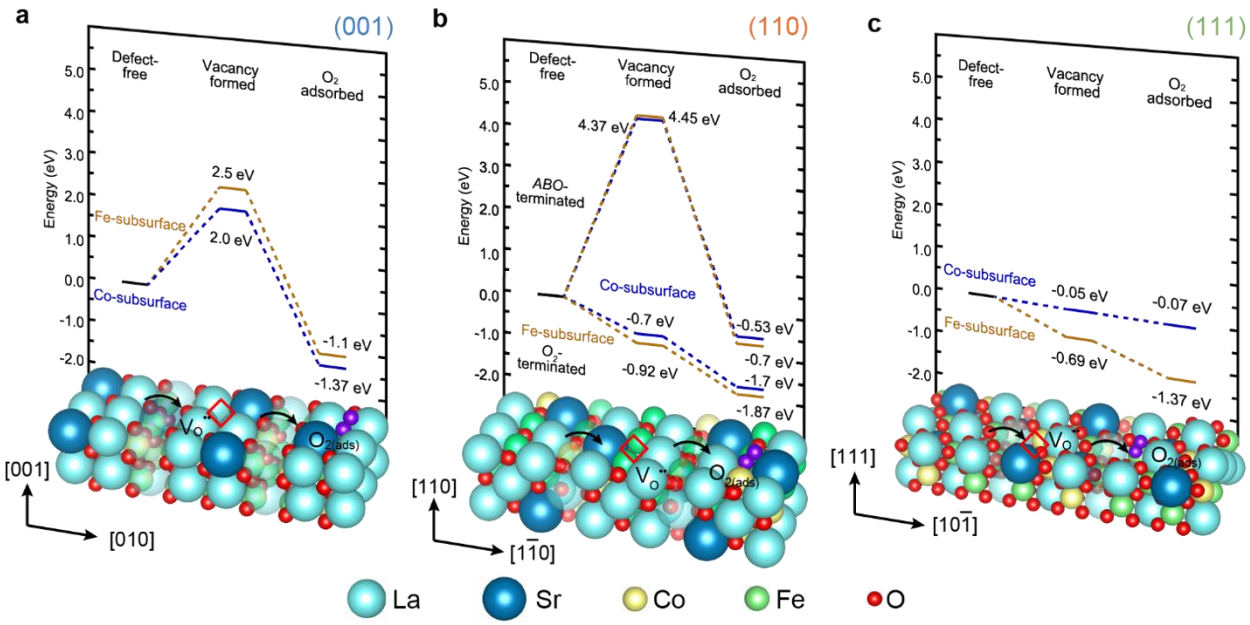

Fig. 4 | First-principles calculations of surface vacancy formation and oxygen adsorption. DFT calculations illustrate the different formation energy for surface vacancies across the (**a**) (001), (**b**) (110) with both *ABO*-termination and O_2-termination, and (**c**) (111) surface variants. Vacancy formation is unfavorable on (001) surfaces and *ABO*-terminated (110) surfaces, whereas (111) and O_2-terminated (110) surfaces have favorable vacancy formation energies.

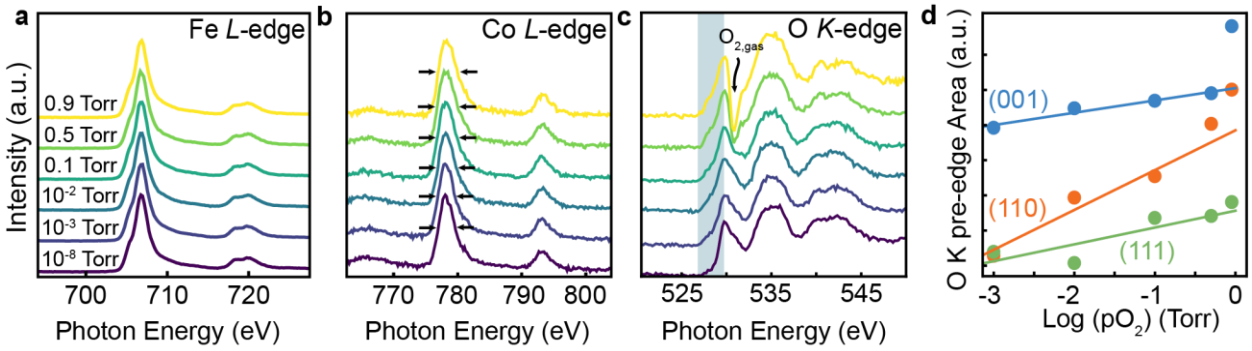

Fig. 5 | Electronic interactions of cathode surfaces. Representative X-ray absorption spectra from (110) surfaces as a function of pressure indicate changing surface electronic structure for the (**a**) iron *L*, (**b**) cobalt *L*, and (**c**) oxygen *K* edges. (**d**) Changing pre-peak area (shaded region in (**c**)) of the oxygen *K* edge is quantified to demonstrate the different propensities for adsorption and charge-transfer on different surfaces, lines are a guide for the eye.

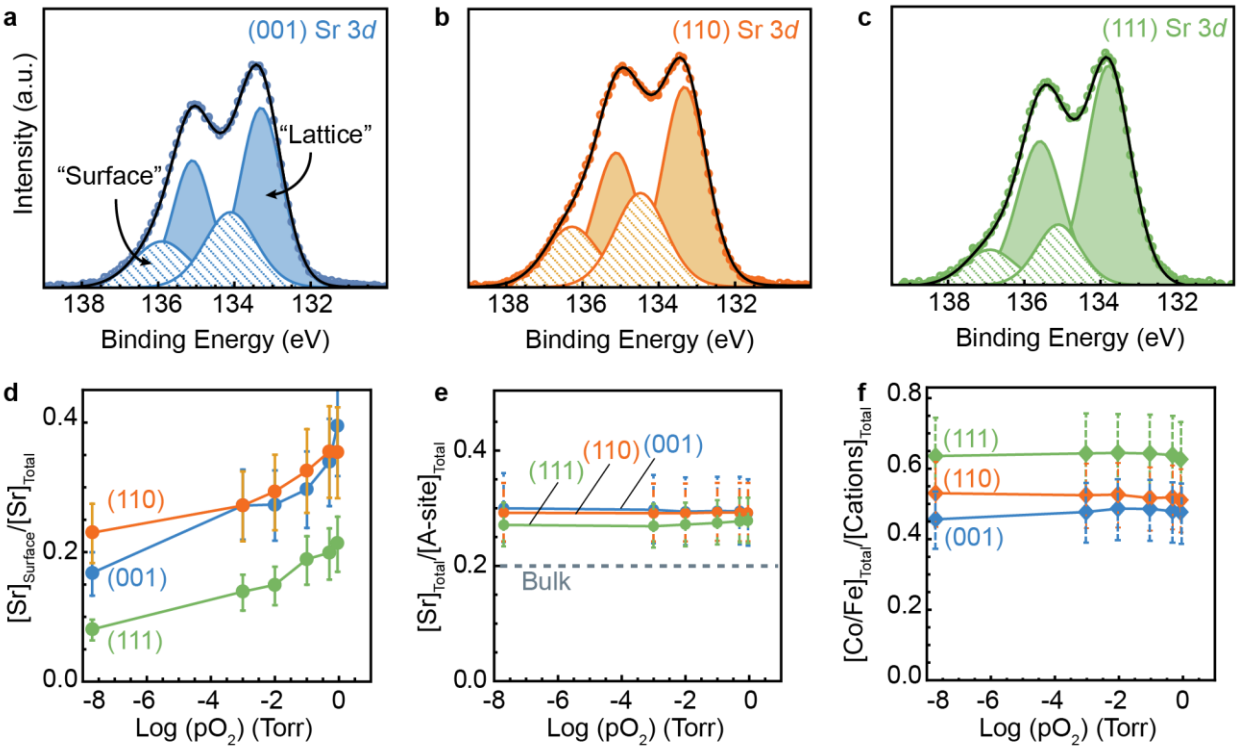

Fig. 6 | Evolution of perovskite surface chemistry. Representative strontium 3*d* spectra for the (**a**) (001), (**b**) (110), and (**c**) (111) surfaces showing the different contributions of "surface" and "lattice" components. (**d**) *In situ* observation of strontium segregation is quantified using the relative intensities of the "surface" and "lattice" components of the strontium 3*d* excitation as a function of gas pressure. (**e**) XPS chemical analysis reveals that the different surface orientations have differing quantities of *B*-site cations in the near-surface region.

1 S. J. Skinner, *Int J Inorg Mater*, 2001, **3**, 113–121.

2 C. Sun, R. Hui and J. Roller, *J Solid State Electr*, 2010, **14**, 1125–1144.

3 J. A. Kilner and M. Burriel, *Mater Res*, 2014, **44**, 365–393.

4 J. Suntivich, H. A. Gasteiger, N. Yabuuchi, H. Nakanishi, J. B. Goodenough and Y. Shao-Horn, *Nat Chem*, 2011, **3**, 546.

5 Z. Shao and S. M. Haile, *Nature*, 2004, **431**, 170.

6 Y.-L. Lee, M. J. Gadre, Y. Shao-Horn and D. Morgan, *Phys Chem Chem Phys*, 2015, **17**, 21643–21663.

7 R. Gao, A. C. P. Jain, S. Pandya, Y. Dong, Y. Yuan, H. Zhou, L. R. Dedon, V. Thoréton, S. Saremi, R. Xu, A. Luo, T. Chen, V. Gopalan, E. Ertekin, J. Kilner, T. Ishihara, N. H. Perry, D. R. Trinkle and L. W. Martin, *Adv Mater*, 2020, **20**, 1905178.

8 M. Kubicek, Z. Cai, W. Ma, B. Yildiz, H. Hutter and J. Fleig, *ACS Nano*, 2013, **7**, 3276–3286.

9 A. Kushima and B. Yildiz, *J Mater Chem*, 2010, **20**, 4809–4819.

10 B. Koo, H. Kwon, Y. Kim, H. G. Seo, J. W. Han and W. Jung, *Energy Environ Sci*, 2017, **11**, 71–77.

11 K. A. Stoerzinger, W. S. Choi, H. Jeen, H. N. Lee and Y. Shao-Horn, *J Phys Chem Lett*, 2015, **6**, 487–492.

12 Y.-L. Lee, J. Kleis, J. Rossmeisl and D. Morgan, *Phys Rev B*, 2009, **80**, 224101.

13 Y. A. Mastrikov, R. Merkle, E. A. Kotomin, M. M. Kuklja and J. Maier, *J Mater Chem A*, 2018, **6**, 11929–11940.

14 C. J. Eom, D.-Y. Kuo, C. Adamo, E. J. Moon, S. J. May, E. J. Crumlin, D. G. Schlom and J. Suntivich, *Nat Comm*, 2018, **9**, 4034.

15 A. R. Akbashev, L. Zhang, J. T. Mefford, J. Park, B. Butz, H. Luftman, W. C. Chueh and A. Vojvodic, *Energy Environ Sci*, 2018, **11**, 1762–1769.

16 K. Kerman, C. Ko and S. Ramanathan, *Phys Chem Chem Phys*, 2012, **14**, 11953–11960.

17 L. Yan, K. R. Balasubramaniam, S. Wang, H. Du and P. A. Salvador, *Solid State Ionics*, 2011, **194**, 9–16.

18 Y. Miyahara, K. Miyazaki, T. Fukutsuka and T. Abe, *Chemelectrochem*, 2016, **3**, 214–217.

19 K. A. Stoerzinger, L. Qiao, M. D. Biegalski and Y. Shao-Horn, *J Phys Chem Lett*, 2014, **5**, 1636–1641.

20 K. A. Stoerzinger, O. Diaz-Morales, M. Kolb, R. R. Rao, R. Frydendal, L. Qiao, X. R. Wang, N. B. Halck, J. Rossmeisl, H. A. Hansen, T. Vegge, I. E. L. Stephens, M. T. M. Koper and Y. Shao-Horn, *ACS Energy Lett*, 2017, **2**, 876-881

21 M. Burriel, J. Peña-Martínez, R. J. Chater, S. Fearn, A. V. Berenov, S. J. Skinner and J. A. Kilner, *Chem Mater*, 2012, **24**, 613–621.

22 S. Fearn, J. C. H. Rossiny, J. A. Kilner and J. R. G. Evans, *Solid State Ionics*, 2012, **211**, 51–57.

23 F. S. Baumann, J. Fleig, H.-U. Habermeier and J. Maier, *Solid State Ionics*, 2006, **177**, 3187–3191.

24 J. Fleig, F. S. Baumann, V. Brichzin, H. -R. Kim, J. Jamnik, G. Cristiani, H. -U. Habermeier and J. Maier, *Fuel Cells*, 2006, **6**, 284–292.

25 J. Fleig, H.-R. Kim, J. Jamnik and J. Maier, *Fuel Cells*, 2008, **8**, 330–337.

26 J. Karthik, A. R. Damodaran and L. W. Martin, *Adv Mater*, 2012, **24**, 1610–1615.

27 G. Kresse and J. Furthmüller, *Comp Mater Sci*, 1996, **6**, 15–50.

28 G. Kresse and J. Furthmüller, *Phys Rev B*, 1996, **54**, 11169–11186.

29 G. Kresse and D. Joubert, *Phys Rev B*, 1998, **59**, 1758–1775.

30 P. E. Blöchl, *Phys Rev B*, 1994, **50**, 17953–17979.

31 J. P. Perdew, K. Burke and M. Ernzerhof, *Phys Rev Lett*, 1996, **77**, 3865–3868.

32 J. Hubbard, *Proc Royal Soc Lond Ser Math Phys Sci*, 1963, **276**, 238–257.

34 M. E. Grass, P. G. Karlsson, F. Aksoy, M. Lundqvist, B. Wannberg, B. S. Mun, Z. Hussain and Z. Liu, *Rev Sci Instrum*, 2010, **81**, 053106.

35 J. E. Readman, A. Olafsen, Y. Larring and R. Blom, *J Mater Chem*, 2005, **15**, 1931–1937.

36 M. Burriel, S. Wilkins, J. P. Hill, M. A. Muñoz-Márquez, H. H. Brongersma, J. A. Kilner, M. P. Ryan and S. J. Skinner, *Energy Environ Sci*, 2013, **7**, 311–316.

37 R. Merkle and J. Maier, *Angewandte Chemie Int Ed*, 2008, **47**, 3874–3894.

38 M. Kubicek, T. M. Huber, A. Welzl, A. Penn, G. M. Rupp, J. Bernardi, M. Stöger-Pollach, H. Hutter and J. Fleig, *Solid State Ionics*, 2014, **256**, 38–44.

39 E. Mutoro, E. J. Crumlin, M. D. Biegalski, H. M. Christen and Y. Shao-Horn, *Energy Environ Sci*, 2011, **4**, 3689–3696.

40 E. J. Crumlin, E. Mutoro, S.-J. Ahn, G. J. la O', D. N. Leonard, A. Borisevich, M. D. Biegalski, H. M. Christen and Y. Shao-Horn, *J Phys Chem Lett*, 2010, **1**, 3149–3155.

41 T. Ishihara, H. Matsuda and Y. Takita, *J Am Chem Soc*, 1994, **116**, 3801–3803.

42 J. A. Lane, S. J. Benson, D. Waller and J. A. Kilner, *Solid State Ionics*, 1999, **121**, 201–208.

43 J. Fleig, R. Merkle and J. Maier, *Phys Chem Chem Phys*, 2007, **9**, 2713.

44 A. Schmid, G. M. Rupp and J. Fleig, *Chem Mater*, 2018, **30**, 4242–4252.

45 S. B. Adler, *Chem Rev*, 2004, **104**, 4791–4844.

46 D. Xu, E. M. Hopper, K.-C. Chang, P. M. Baldo, H. Park, J. A. Eastman, H. You, P. H. Fuoss, B. J. Ingram and P. Zapol, *J Power Sources*, 2020, **451**, 227478.

47 W. Lee, J. W. Han, Y. Chen, Z. Cai and B. Yildiz, *J Am Chem Soc*, 2013, **135**, 7909–7925.

48 A. Staykov, H. Téllez, T. Akbay, J. Druce, T. Ishihara and J. Kilner, *Chem Mater*, 2015, **27**, 8273–8281.

49 M. Abbate, F. M. F. de Groot, J. C. Fuggle, A. Fujimori, O. Strebel, F. Lopez, M. Domke, G. Kaindl, G. A. Sawatzky, M. Takano, Y. Takeda, H. Eisaki and S. Uchida, *Phys Rev B*, 1992, **46**, 4511–4519.

50 M. Abbate, J. C. Fuggle, A. Fujimori, L. H. Tjeng, C. T. Chen, R. Potze, G. A. Sawatzky, H. Eisaki and S. Uchida, *Phys Rev B*, 1992, **47**, 16124–16130.

51 M. Merz, P. Nagel, C. Pinta, A. Samartsev, H. v. Löhneysen, M. Wissinger, S. Uebe, A. Assmann, D. Fuchs and S. Schuppler, *Phys Rev B*, 2010, **82**, 174416.

52 Y. Orikasa, T. Ina, T. Nakao, A. Mineshige, K. Amezawa, M. Oishi, H. Arai, Z. Ogumi and Y. Uchimoto, *Phys Chem Chem Phys*, 2011, **13**, 16637–16643.

53 D. N. Mueller, M. L. Machala, H. Bluhm and W. C. Chueh, *Nat Comm*, 2015, **6**, 6097.

54 N. Tsvetkov, Q. Lu, L. Sun, E. J. Crumlin and B. Yildiz, *Nat Mater*, 2016, **15**, 1010–1016.

55 Y. Chen, H. Téllez, M. Burriel, F. Yang, N. Tsvetkov, Z. Cai, D. W. McComb, J. A. Kilner and B. Yildiz, *Chem Mater*, 2015, **27**, 5436–5450.

56 H. Wang, K. J. Yakal-Kremski, T. Yeh, G. M. Rupp, A. Limbeck, J. Fleig and S. A. Barnett, *J Electrochem Soc*, 2016, **163**, F581–F585.

57 E. J. Crumlin, E. Mutoro, Z. Liu, M. E. Grass, M. D. Biegalski, Y.-L. Lee, D. Morgan, H. M. Christen, H. Bluhm and Y. Shao-Horn, *Energy Environ Sci*, 2012, **5**, 6081–6088.

58 F. Pişkin, R. Bliem and B. Yildiz, *J Mater Chem A*, 2018, **6**, 14136–14145.

59 J. J. Yeh and I. Lindau, *Atom Data Nucl Data*, 1985, **32**, 1–155.

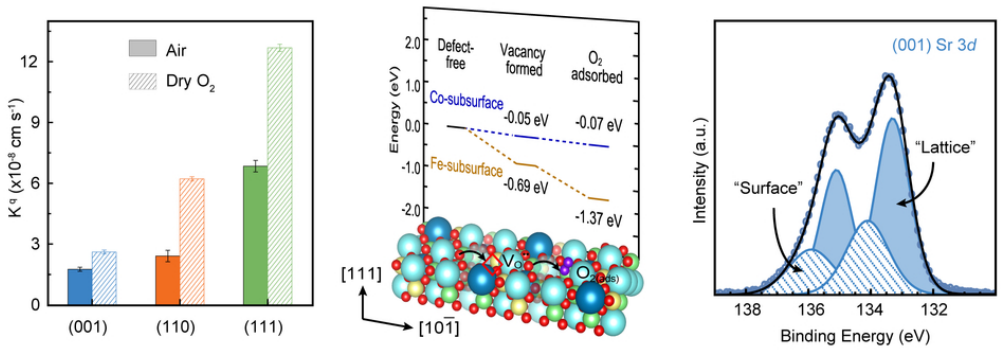

80x40mm (300 x 300 DPI)

Supplementary Information

Ran Gao[1*], Abel Fernandez[1*], Tanmoy Chakraborty[2], Aileen Luo[1], David Pesquera[1,3], Sujit Das[1], Gabriel Velarde[1], Vincent Thoréton[4], John Kilner[4,5], Tatsumi Ishihara[4], Slavomír Nemšák[6], Ethan J. Crumlin[6], Elif Ertekin[7], Lane W. Martin[1,8,#]

[1] Department of Materials Science and Engineering, University of California, Berkeley, Berkeley, CA 94720, USA
[2] Beckman Institute for Advanced Science and Technology, University of Illinois at Urbana−Champaign, Urbana, Illinois 61801, USA
[3] Catalan Institute of Nanoscience and Nanotechnology, Campus UAB, Bellaterra, 08193 Barcelona, Spain
[4] WPI International Institute for Carbon-Neutral Energy Research (WPI-I2CNER), Kyushu University, Fukuoka 81-0395, Japan
[5] Department of Materials, Imperial College London, London SW72AZ, UK
[6] Advanced Light Source, Lawrence Berkeley National Laboratory, Berkeley, CA 94720, USA
[7] Department of Mechanical Science and Engineering, University of Illinois, Urbana-Champaign, Urbana, IL 61801, USA

[8] Materials Sciences Division, Lawrence Berkeley National Laboratory, Berkeley, CA 94720, USA
* These authors contributed equally to this work.
# Corresponding author: lwmartin@berkeley.edu

I. Electrochemical-measurement setup

Electrochemical-impedance-spectroscopy measurements were carried out in a home-built, tube-furnace-based measurement setup (Supplementary Fig. 1). An alumina tube was sealed using KF flanges on both ends, with one end connected to a mechanical pump and the other with a customized KF-type flange through which we accomplished sample connection, gas inlet, and temperature monitoring. An alumina bar is mounted on the flange to hold the sample which is gold-wire-bonded to a CERDIP chip carrier, and four silver wires with thermal shields were used to connect the chip carrier with external BNC ports via electrical feedthroughs. A PARSTAT 3000 potentiostat was used to perform the electrochemical-impedance-spectroscopic measurements. For temperature control, an additional thermocouple was placed immediately adjacent to the sample

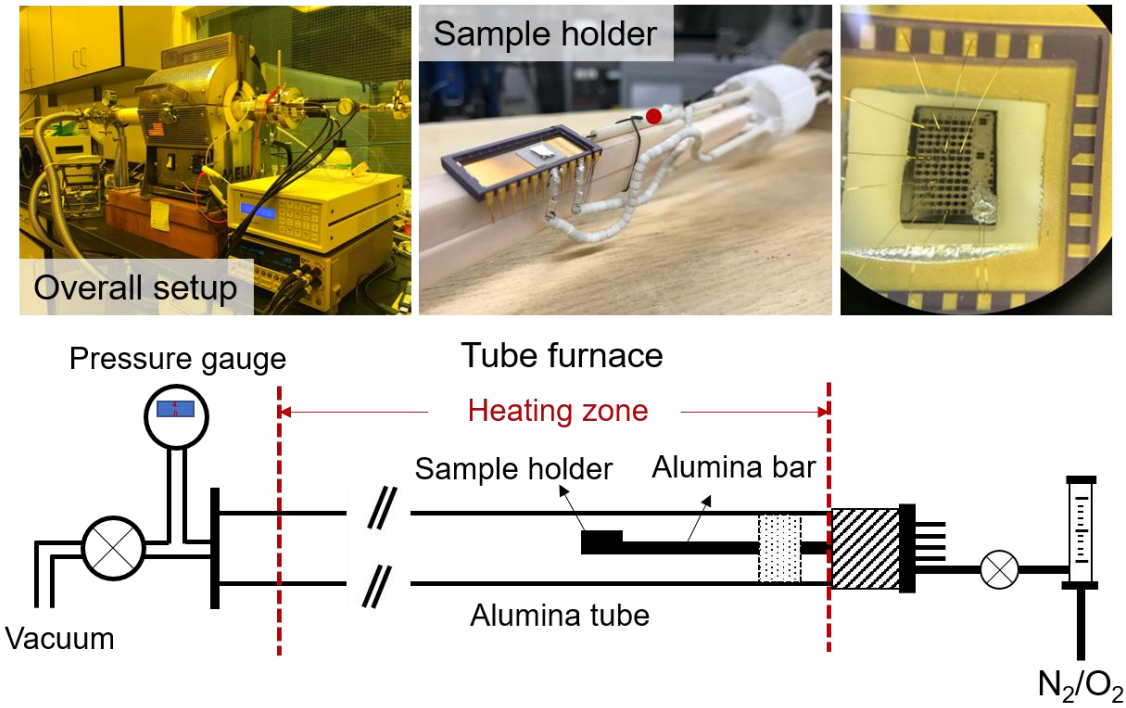

Supplementary Figure 1 | Details of the electrochemical measurement setup. The overall setup is based on a tube furnace (top left) with a custom sample holder (top middle) upon which a ceramic chip carrier enables the mounting and wire-bonded connection of the sample (top right) for measurement. A schematic cross-section view of the measurement setup (bottom) shows the setup and gas-flow direction (from right to left).

holder to measure temperature near the sample surface. During the measurement, the temperature is monitored via the internal thermocouple mounted in proximity to the chip carrier and the PID settings of the furnace were properly tuned to maintain steady temperatures for such a sample geometry. Oxygen-partial pressure was controlled by fixing the inlet flow of oxygen (flow rate at 4 sccm), while the outlet pumping speed was adjusted by changing the opening of the outlet pumping port to achieve the target pressure. Using this setup, pressure control from 80 mTorr to 760 Torr is achievable. Before measuring the samples were allowed to equilibrate at each pressure and temperature for 20 minutes.

II. Half-cell fabrication

Fabrication of the half-cell structures was carried out via a series of pulsed-laser deposition and photolithography steps (Supplementary Fig. 4). Initially, a bilayer consisting of the $SrRuO_3$

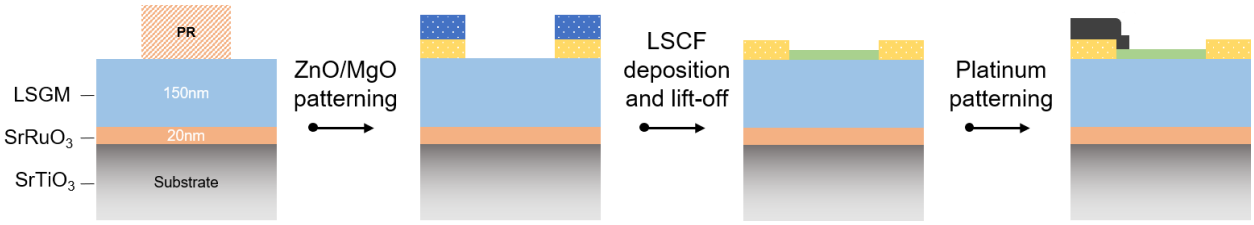

Supplementary Figure 2 | Schematic of the fabrication process for epitaxial half-cell samples.

counter-electrode layer and the LSGM electrolyte are synthesized *in situ*. The resulting heterostructures are removed from the deposition chamber and photolithographically patterned. The photoresist is used to define an amorphous ZnO/MgO insulating layer, deposited at room-temperature via pulsed-laser deposition. The photoresist is subsequently removed leaving behind a hard-mask of ZnO/MgO, which now serves to define the circular LSCF electrodes[1]. The bilayer with patterned hard-mask is reinserted into the pulsed-laser-deposition chamber and subsequent high-temperature deposition is used to grow the LSCF top electrode. The excess and unwanted LSCF (*i.e.*, that not in the circular capacitor areas) is removed via liftoff of the ZnO layer through a NaOH etch which selectively dissolves the ZnO, leaving behind the MgO-insulating layer, and the circular electrodes of LSCF. A final photolithography step is performed to define the platinum pads which are used for wire-bonded electrical connection to the LSCF electrode. Lift-off of the excess photoresist and platinum leaves the completed half-cell structures.

III. Thin-film growth and characterization

Films used in this study were synthesized via pulsed-laser deposition and several studies were carried out to characterize the quality of the thin films. In addition to X-ray Diffraction studies, we performed atomic force microscopy to examine the surface topography of the films with different surface orientations (Supplementary Fig. 3). The surface of the LSCF electrodes was also probed via atomic force microscopy (AFM) to ensure smooth surfaces were obtained, and no extrinsic contributions from differences in surface roughness or secondary phases were influencing the results of the electrochemical measurements (Supplementary Fig. 1e-g).

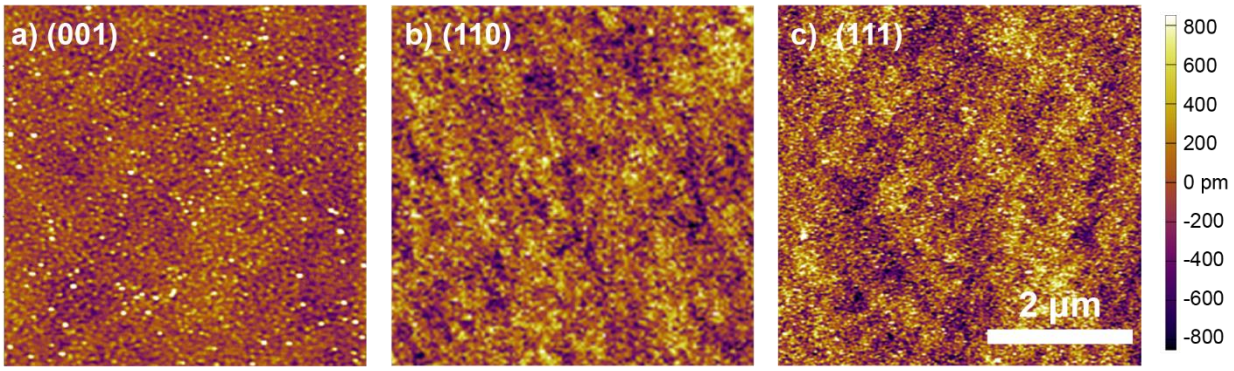

Supplementary Figure 3 | Atomic force microscopy of LSCF thin films. Surface topography scans of (a) (001)-, (b) (110)-, and (c) (111)-oriented LSCF thin films show smooth surfaces for all three surface orientations with no evidence of secondary phases or faceting, and comparable root-mean-square roughness.

Low-energy ion-scattering (LEIS) measurements (Supplementary Fig. 4) were performed to understand the surface-termination of the as-grown LSCF films. The films are predominantly *A*-site terminated for all three surface variants as expected based on previous studies of perovskite terminations [2–4]. Only the (111)-terminated film shows evidence of a small concentration of surface *B*-site cations.

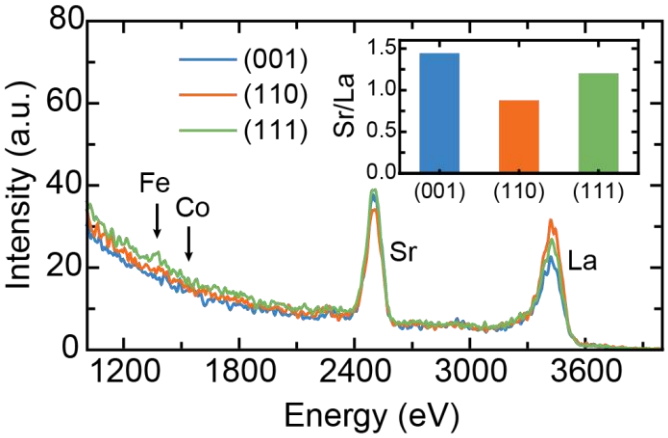

Supplementary Figure 4 | Low-energy ion-scattering (LEIS) measurements. LEIS studies were undertaken to compare the as-grown surface chemistries of the different LSCF surface orientations. All three orientations were found to have *A*-site-rich terminations, with only the (111) surfaces showing any evidence of surface *B*-site cations, *Inset* shows the calculated ration of surface strontium to lanthanum ratio and reveals that all surfaces are non-stoichiometric and have high levels of surface strontium.

Reciprocal-space maps of the tri-layer heterostructures with different surface orientations verify that all the layers are epitaxially strained to the $SrTiO_3$ substrates, eliminating possible contributions from varying strain state to the observed differences in electrochemical reactivity (Supplementary Fig. 5). Owing to the different surface orientations, distinct diffraction conditions were probed to obtain information about the in-plane configuration of the heterostructures.

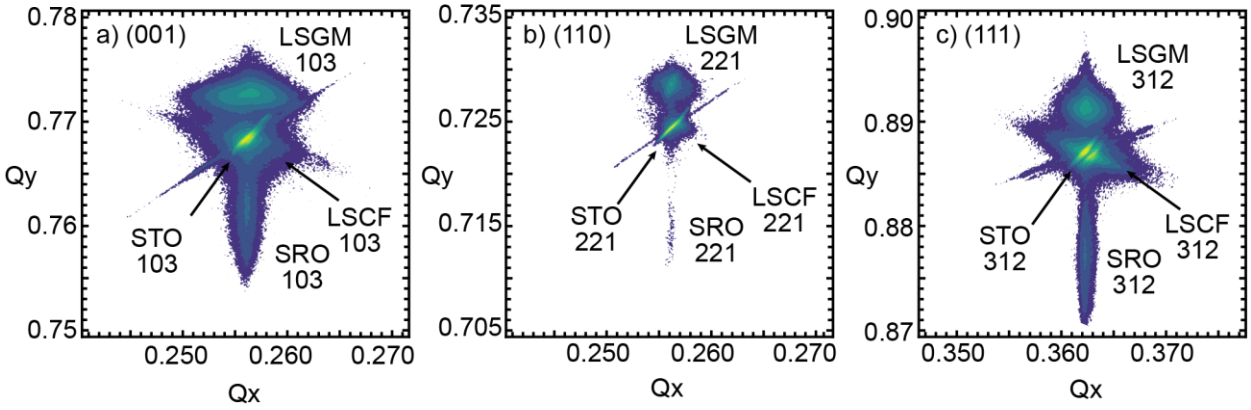

Supplementary Figure 5 | Reciprocal space maps of half-cell heterostructures. Reciprocal-space maps about off-axis diffraction peaks reveal epitaxial relationship and fully strained LSGM electrolyte and $SrRuO_3$ counter-electrode layers for (a) (001)-, (b) (110)-, and (c) (111)-oriented heterostructures.

IV. Half-cell Validation

While previous studies have described the validity of microelectrode designs[5–7], we performed several verification measurements using the as-described measurement setup to ensure our chosen geometry allows for isolation of the surface-reaction impedance. First, we confirm that the surface impedance, R_s, that is extracted is truly related to the oxygen reaction at the surface of the LSCF electrodes. In this case, covering the surface of the LSCF with an oxygen impermeable layer should serve to dramatically increase the surface-reaction impedance, by preventing interaction of the LSCF with the oxygen environment. Using a platinum blocking layer over the surface of the LSCF electrode, we observed an increase in R_s by almost an order of magnitude, indicating that the LSCF surface is indeed redox active (Supplementary Fig. 6a). Additionally, we aimed to ensure that the majority of the potential drop across the half-cell occurs at the LSCF-gas

interface, and that the measured impedance directly reflects this polarization resistance rather than diffusion processes in the LSGM electrolyte. The total electrical resistance of the half-cell device was directly related to the high-frequency intercept in a Nyquist plot. In the case of diffusion in the electrolyte contributing significantly to the measured impedance, we should observe a strong dependence of the high-frequency intercept on the LSGM thickness as is the case for a platinum electrode on the LSGM (Supplementary Fig. 6b). With an exposed LSCF electrode, however, we see no dependence on LSGM thickness, indicating that the surface-reaction is the limiting impedance in the half-cell, and that these devices adequately isolate the surface reaction for further study. Finally, it well known that the electrode-electrolyte-atmosphere triple-phase boundaries serves as the main reaction site for many cell geometries owing to enhanced ionic diffusion of reduced species. With good mixed-ionic-electronic conductors, in a thin-film geometry, the diffusion of oxygen anions no longer is a limiting factor and the reaction truly occurs at the

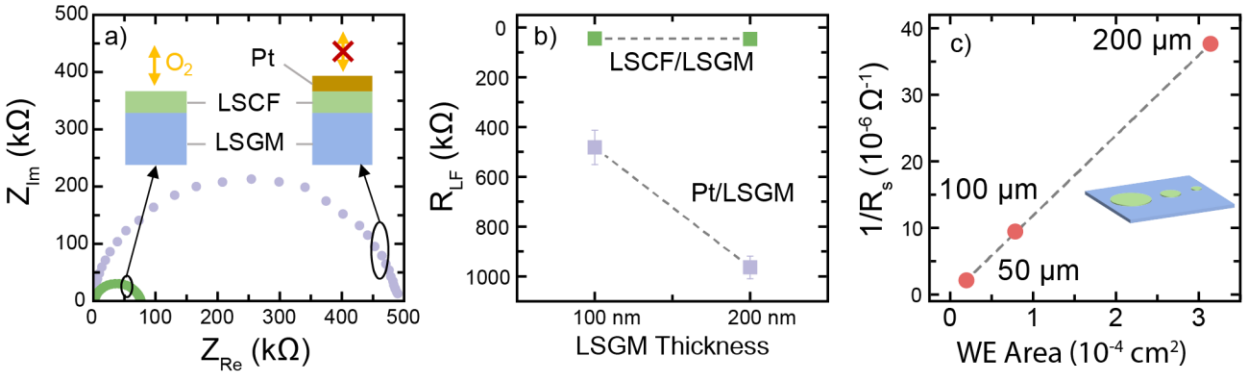

Supplementary Figure 6 | Validation of the epitaxial half-cell heterostructures. (**a**) Comparison of an impedance measurement of the half-cell and one where the LSCF has been covered by a thin, platinum blocking layer reveals a large increase in the surface impedance when the LSCF surface is isolated from the gas environments, confirming that the LSCF is redox active. (**b**) Comparison of the low-frequency intercept of the Nyquist plot (R_{LF}) between a half-cell device under study and one where platinum replaces the LSCF layer. The high-frequency intercept in a Nyquist-plot is related to the ohmic drop across the entire device. The large change in the Pt/LSGM impedance with increased LSGM thickness is expected when the majority of the ohmic drop is across the electrolyte layer. The half-cells under investigation show little to no change when the LSGM thickness is increased, confirming that most of the potential drop occurs across the LSCF-gas interface rather than the LSGM thickness, and the ionic diffusion in the LSGM is not contributing to the measured impedance. (**c**) Area dependence of R_s is used to understand the contribution from the triple-phase boundaries in these devices. The linear increase in R_s with increasing working electrode area shows that the measured reaction rate is a property of the surface and not the LSCF/LSGM/gas triple-phase boundary.

electrode surface. This can be seen in the area dependence of the impedance R_s. We observed a linear scaling of R_s with electrode area (Supplementary Fig. 6c), indicating the active sites for oxygen reaction are at the exposed LSCF surface and triple-phase boundaries provide negligible contribution to the measured impedance.

IV. p_{O_2}-dependent impedance spectroscopy

The results of p_{O_2}-dependent impedance-spectroscopy studies are presented in the main text. Representative Nyquist plots obtained for such p_{O_2}-dependent measurements on the three surface variants are presented here (Supplementary Fig. 7). The increasing R_s with decreasing p_{O_2} can be observed in the progressively increasing low-frequency intercept. For a given pressure, the (111) surface produces significantly smaller R_s values at all pressures studied. It can be seen, that the high-frequency intercept remains constant for all measurements except for the very lowest pressures measured where a small shoulder appears. The origin of this shoulder was not studied

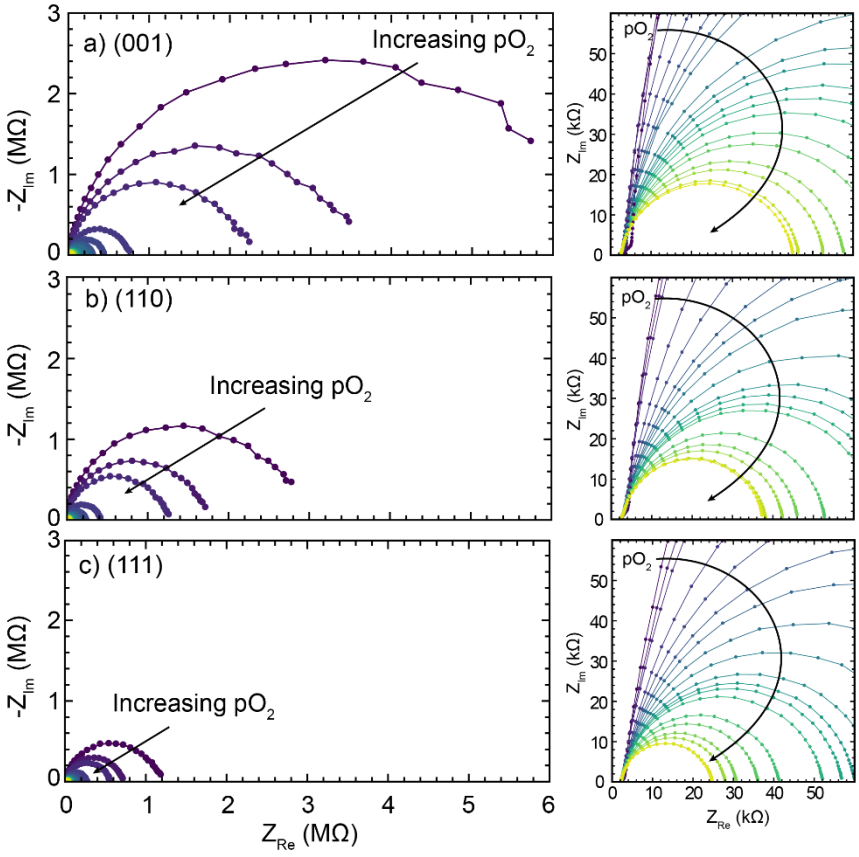

Supplementary Figure 7 | Nyquist plots from p_{O_2}-dependent impedance spectroscopy studies. Pressure-dependent studies for (**a**) (001), (**b**) (110), and (**c**) (111) surfaces reveal a decrease in the high-frequency intercept as p_{O_2} is increased. The low-frequency intercept does not change until the lowest pressure, indicating that the half-cell geometry nicely isolates the surface-reaction process at pressure of interest. The right graph shows a zoom-in of the low-frequency range. The electrochemical reaction rate between the different surfaces can be observed to increase from the decreasing high-frequency intercepts from (001) to (110) to (111) surfaces.

in-depth here, but maybe related to the decreasing oxygen conductivity of the electrode at reduced oxygen pressures, adding an additional contribution to the half-cell impedance.

V. Ambient-pressure X-ray photoelectron and absorption spectroscopy

Spectroscopic studies were performed as a function of oxygen pressure at 350°C at beamline 9.3.2 of the Advanced Light Source. Prior to measurement, samples were cleaned in 10 mTorr of gaseous oxygen at 350°C for 15 min. while observing the carbon 1*s* excitation to ensure carbonaceous contaminants were removed. A representative spectrum of the carbon 1*s* peak is presented (Supplementary Fig. 8) and shows no carbon 1*s* peak, which appears at >284 eV depending on the type of contaminant. The only peak observed in this range is a weak peak from the strontium 3*p* 1/2 excitation, confirming samples were appropriately cleaned prior to measurement. Spectra for the oxygen *K*- (Supplementary Fig. 9), cobalt *L*- (Supplementary Fig. 10), and iron *L*-edge (Supplementary Fig. 11) absorptions for all orientations present qualitatively similar behavior as a function of oxygen pressure. Difference curves obtained by subtracting a given spectrum from the low pressure (10^{-8} Torr) spectrum were used to better visualize the change in absorption with increasing pressure.

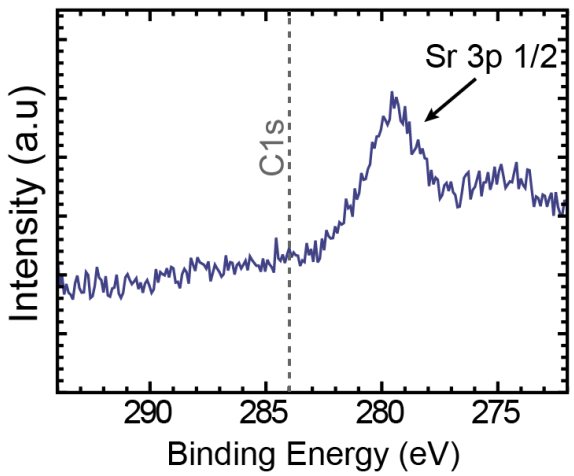

Supplementary Figure 8 | XPS measurements after sample cleaning. Measurements in the range of the carbon 1*s* excitation post-cleaning procedure reveals no adventitious or carbonaceous contamination on the surface of the samples prior to AP-XAS and AP-XPS measurements.

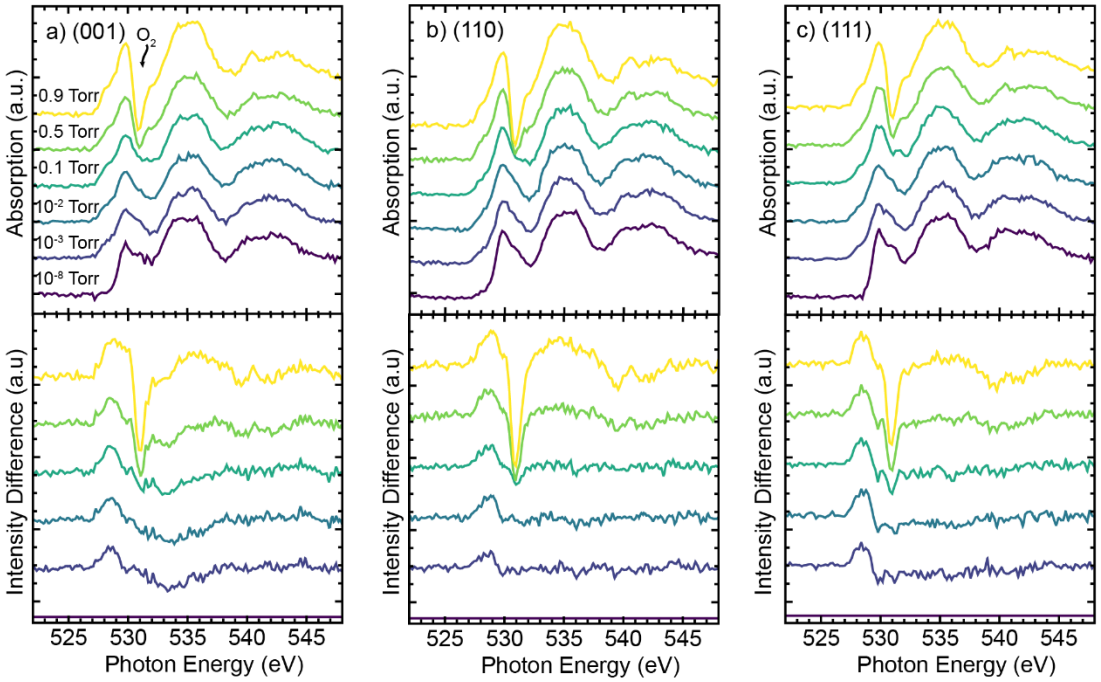

Supplementary Figure 9 | p_{O_2}-dependent XAS measurements of the oxygen *K* edge. Studies for the (**a**) (001), (**b**) (110), and (**c**) (111) surfaces reveals that the different surface variants exhibit a change in the pre-peak intensity around 528 eV with increasing p_{O_2}. The bottom panel shows the difference curves for each pressure with respect to XAS measured at 10^{-8} Torr. The changing pre-peak intensity shows up as an emerging peak at 528 eV. The large dip at 531 eV is due to gaseous O_2 in the measurement chamber.

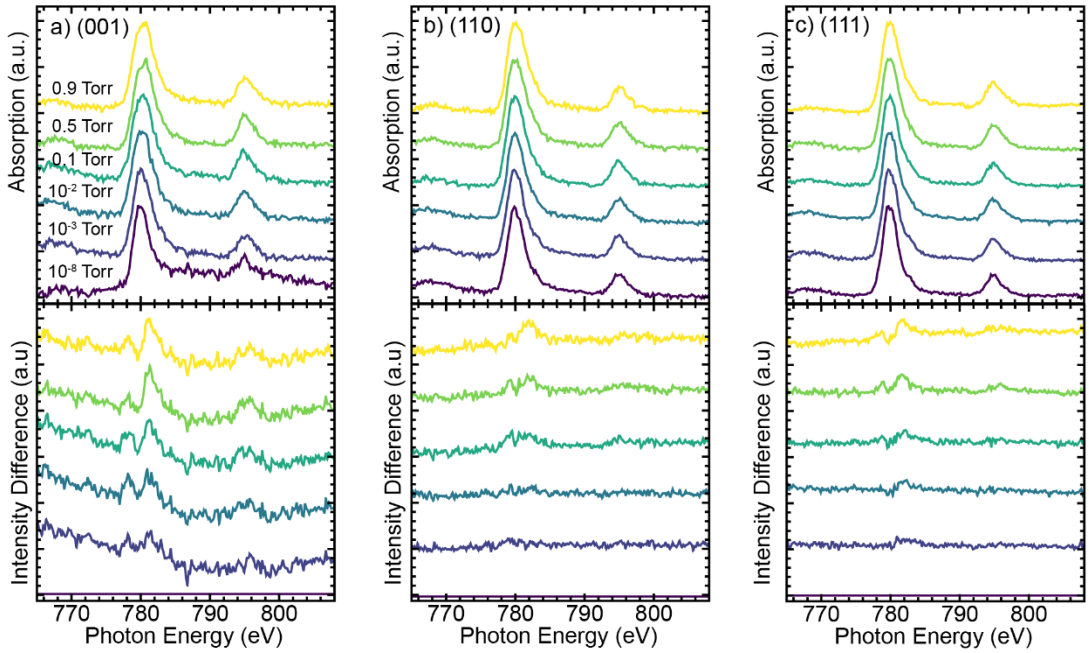

Supplementary Figure 10 | p_{O_2}-dependent XAS measurements of the cobalt *L* edge. Studies for the (**a**) (001), (**b**) (110), and (**c**) (111) surfaces reveal a changing oxidation state with increasing p_{O_2}. The initial cobalt appears to be mainly 3+, and increasing width indicates the partial oxidation to 4+ valence. The bottom panel shows the difference curves for each pressure with respect to XAS measured at 10^{-8} Torr. The difference curves illustrate the change in oxidation state as two peaks that appear on either side of the cobalt white line at ~780 eV.

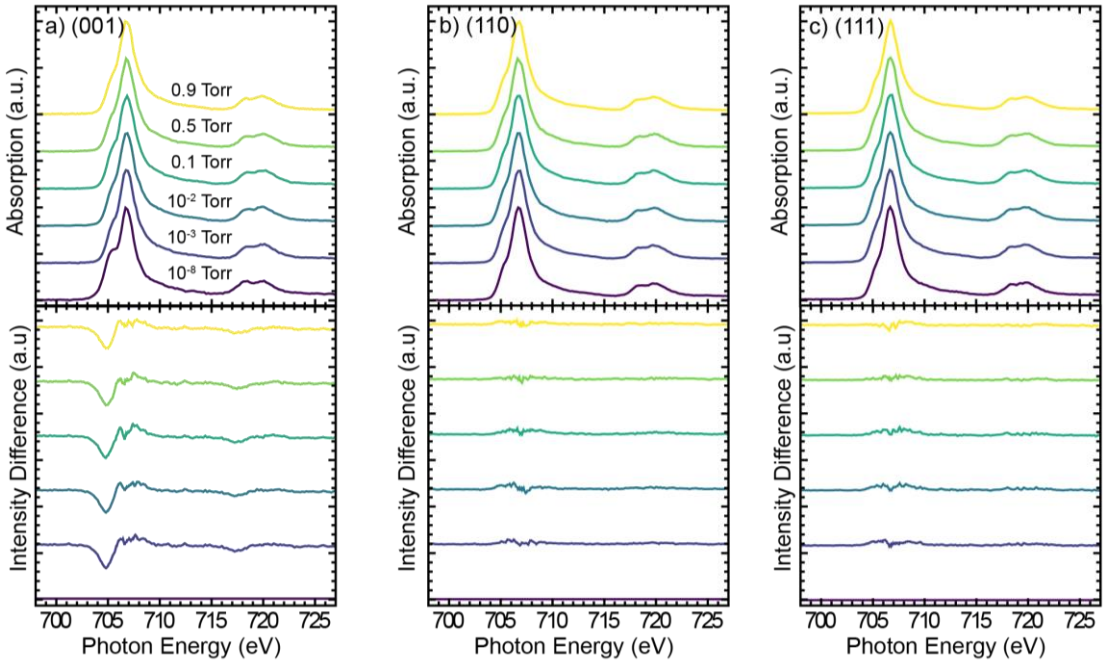

Supplementary Figure 11 | p_{O_2}-dependent XAS measurements of the iron *L* edge. Studies for the (**a**) (001), (**b**) (110), and (**c**) (111) surfaces reveal little to no change in oxidation state with increasing p_{O_2}. A low-energy shoulder is observed in the measurement of the (001) surface at 10^{-8} Torr, but this shoulder disappears after reaching 1 mTorr and subsequent scans show no further change. The origin of this shoulder is unclear, but may be due to some reduction of Fe^{3+} to Fe^{2+} after heating in UHV conditions, which is then recovered after introduction of sufficient pressures of oxygen. The bottom panel shows the difference curves for each pressure with respect to XAS measured at 10^{-8} Torr. The difference curves illustrate the minimal change in oxidation state.

In the oxygen *K*-edge spectra (Supplementary Fig. 9), a clear peak at ~528 eV appears with increasing p_{O_2}. The area of this peak was integrated to obtain a quantitative understanding of the hole doping associated with O_2-adsorption. The cobalt *L*-edge (Supplementary Fig. 10) shows slight changes with increasing p_{O_2}, related to oxidation of some Co^{3+} to Co^{4+}. The differences in signal-to-noise ratio between the different surface orientation are likely a reflection of the quantity of cobalt atoms in the probed region. As revealed by the XPS measurements, the (111) surface has more near-surface *B*-site cations, producing cleaner XAS spectra compared to the (110) and, particularly, the (001) surfaces. The iron *L*-edge (Supplementary Fig. 11) shows no change for the three orientations, with the exception of a shoulder that appears at the lowest pressures in the (001) surfaces. This shoulder disappears upon introduction of some oxygen, with no further change upon further increasing p_{O_2}. With no further change at higher p_{O_2} this shoulder is likely the result of

some small fraction of Fe^{2+} remaining near the surface of the as-grown film, which is oxidized upon exposure to O_2.

Photoelectron excitations were also measured in ambient conditions to understand the near surface chemistry of the three different orientations. All spectra were aligned to the low binding energy peak of the lanthanum 4*d* photoemission peak, which is typically not sensitive to oxygen pressure, and resulted in the valence-band edge being located at 0 eV, as is expected for the metallic nature of LSCF at elevated temperatures[8]. The probe depth of these measurements, at an excitation energy of 670 eV, was calculated to be ~1.3 nm, using the NIST Inelastic Mean-Free Path Database[9]. Representative spectra for the four core-level excitations under investigation show similar peak shapes among the different orientations with some small exceptions (Supplementary Fig. 12). The oxygen 1*s* emission peak was fit using two or three components, similar to previous studies on perovskite cathodes[10]; however, in this study we focus on the cation stoichiometry[12,13].

The strontium 3*d* peak was fit with four components, as typically done with *A*-site cation emission peaks. Spin-orbit splitting introduces a 3/2-5/2 doublet, which are fit using a fixed branching ratio of 3:2 and a binding energy shift of the +1.8 eV for the 3/2 component relative to the 5/2 component[10,11]. The strontium 3*d* peak is fit with low-binding-energy (LBE) and high-binding-energy (HBE) doublets. The HBE doublet has been observed in many different strontium-containing samples, but the precise origin is still under investigation[12]. Many reports attribute the HBE doublet to "surface" species, be it surface-terminated strontium, or secondary strontium-based phases that form at surfaces[10,13,14]. In this study, we adopt the "surface-like" attribution of the HBE doublet, owing to the similarity with previous studies, and the changing contributions from the "surface-like" and "lattice-like" species observed during the measurement, as would be

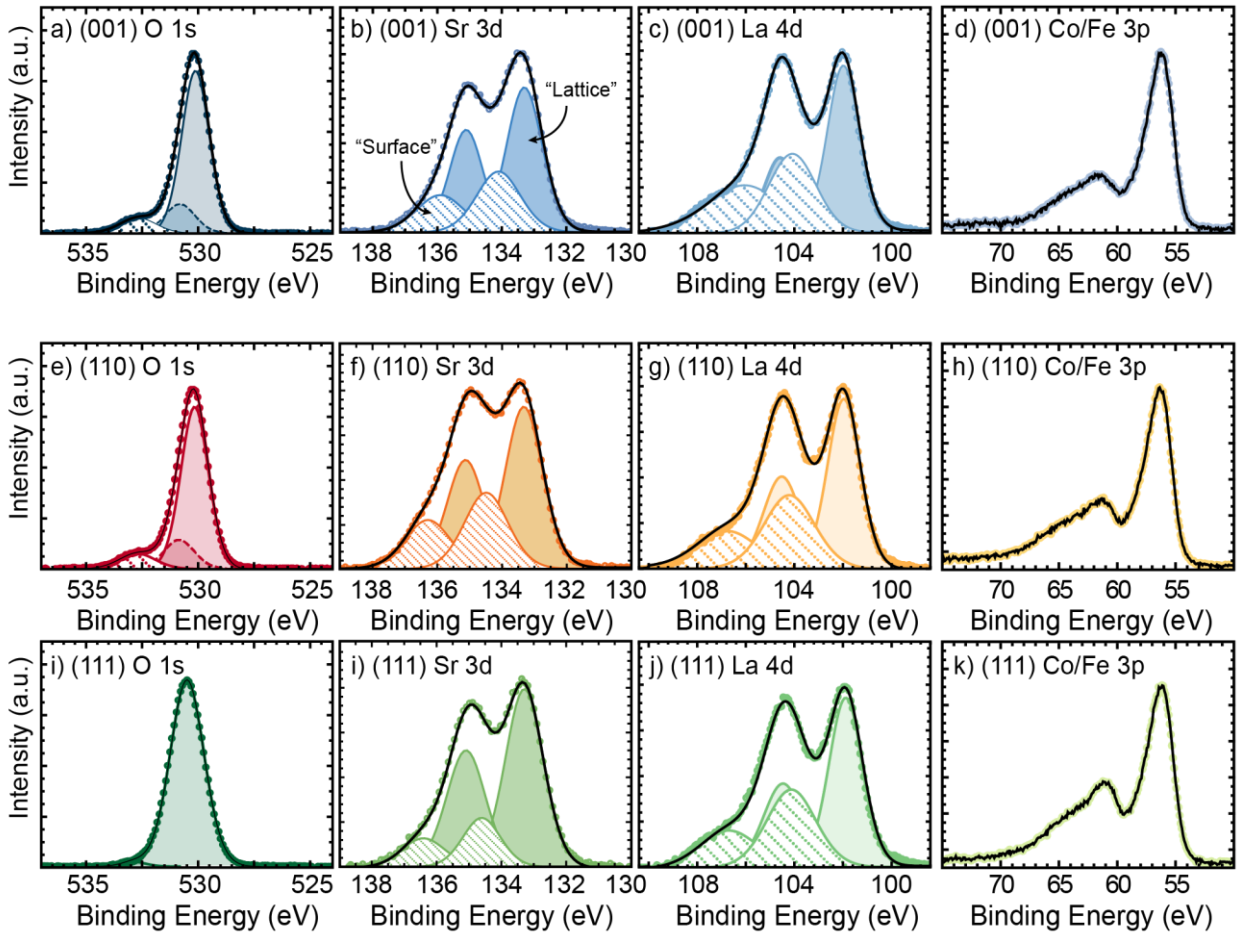

Supplementary Figure 12 | Representative spectra of the four main core-level excitations. This study focused on four different core-level excitations for the three surface orientations including the oxygen 1*s*, strontium 3*d*, lanthanum 4*d*, and cobalt/iron 3*p* levels for (a-d, respectively) (001), (e-h, respectively) (110), and (i-k, respectively) (111) surfaces. All three surfaces show qualitatively similar spectra. The oxygen 1*s* spectra for all three surfaces were fit using a "surface" and "lattice" component, with the relative intensity corresponding well with the relative intensity of strontium "surface" and "lattice" components. The (001) and (110) oxygen 1*s* spectra were fit with a third component, occasionally attributed to M-O bond of unknown origin; however, this component was not needed to obtain a good fit for the (111) surface. The complex splitting of transition metal 3*p* states and the overlapping of the cobalt and iron 3*p* excitations prevented any meaningful insight to be gained from fitting of components of those states. As such, the integrated area of the entire peak was used to quantify the overall *B*-site cation chemistry at the surface.

expected for strontium-segregation at elevated temperatures. The difference in the magnitude of the "surface-like" component between the different surface orientations can be clearly seen (Supplementary Fig.12). The p_{O_2}-dependence of the relative "surface-like" and "lattice-like" contributions were calculated by taking the total area of the "surface-like" components over the total area of the strontium 3*d* excitation for each spectra measured at each pressure (Supplementary

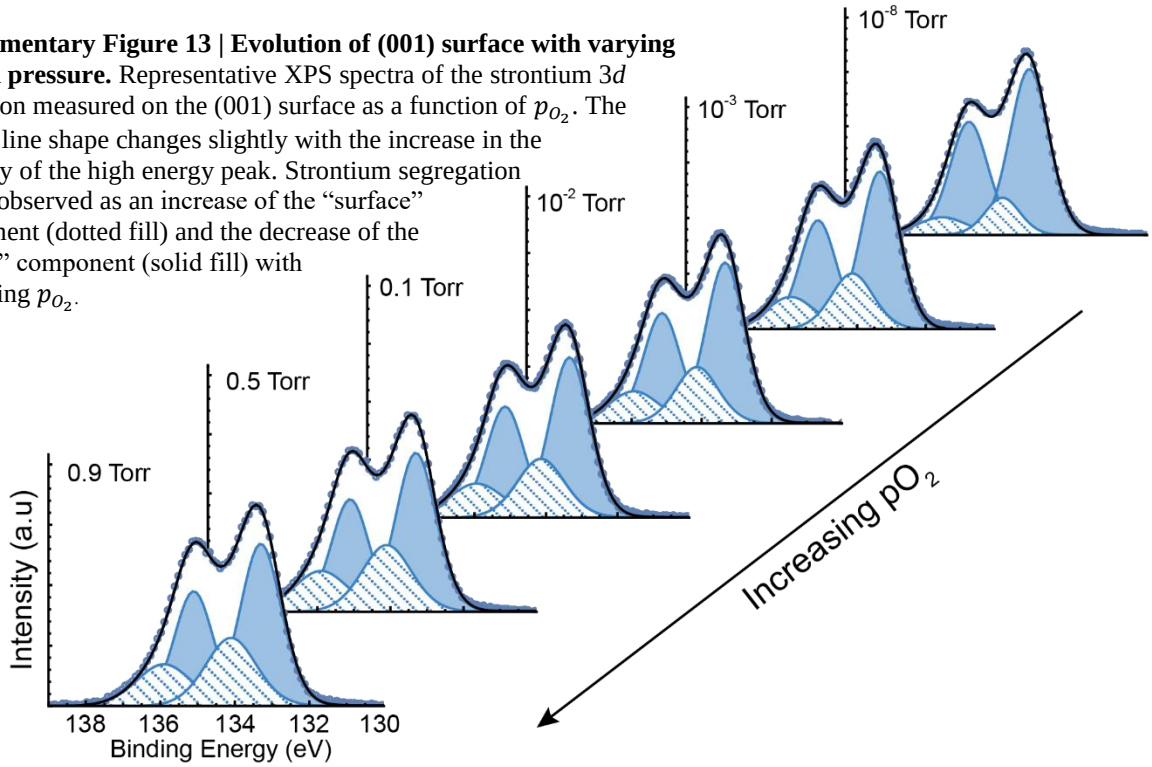

Supplementary Figure 13 | Evolution of (001) surface with varying oxygen pressure. Representative XPS spectra of the strontium 3*d* excitation measured on the (001) surface as a function of p_{O_2}. The overall line shape changes slightly with the increase in the intensity of the high energy peak. Strontium segregation can be observed as an increase of the "surface" component (dotted fill) and the decrease of the "lattice" component (solid fill) with increasing p_{O_2}.

Fig. 13). The lanthanum 4*d* photoemission peak was treated in a similar manner with a branching ratio of 3:2 for the 5/2-3/2 doublet and a binding energy shift of 2.8 eV[15]. The lanthanum 4*d* excitation also shows the presence of overlapping LBE and HBE doublets. These doublets may also be related to "surface-like" and "lattice-like" species, in the same manner as the strontium 3*d* excitation; however, the lanthanum 4*d* excitations are known to involve other final-state and plasmon effects that complicate quantitative extraction[15]. The cobalt/iron 3*p* has a complex line shape due to the various possible photoemission peaks and the possible overlapping of the cobalt and iron contributions. Accurately fitting such transition-metal excitations is known to involve many components, which dramatically reduces the confidence in extracting any meaningful insight from individual contributions[16,17]. Owing to the difficulty in assigning precise origins to the various components in the cobalt/iron 3*p* excitation, and the open debate regarding the origin of the LBE/HBE doublets in the lanthanum 4*d* and strontium 3*d* excitations, we focus on the total area of each excitation. In this study, the total area of the combined cobalt/iron 3*p* peak was used to

calculate the relative ratio of *B*-site cations in the near-surface region. For normalization using the photoionization cross-section, the iron and cobalt contributions were separated at 59.5 eV. The peak area integrated above 59.5 eV was normalized using the cobalt photoionization cross-section of 0.17 and the area below 59.5 eV was normalized using the iron photoionization cross-section of 0.15. While there is likely some additional error in the quantification of the *B*-site concentration induced by the potential overlapping of iron and cobalt peaks, as well as differences in the information depth of the cobalt/iron 3*p* excitation compared to the lanthanum 4*d* and strontium 3*d* excitation, our goal is to evaluate the differences between the different surface orientations rather than obtain precise quantitative compositions. Thus, we believe the trends observed between the different surface orientations are still valid. To support the validity of these quantitative analyses, we calculated the strontium-to-lanthanum ratio in the near-surface regime, using the total integrated area from the strontium 3*d* and lanthanum 4*d* excitations, normalized by their respective photoionization cross-sections (0.7 and 0.5, respectively), and provide an estimation of the *A*-site stoichiometry in the probed region. The ideal, bulk ratio is expected to be 0.2, and the measured ratio (main text, Fig. 6e) is shown to be ~0.30, indicating good agreement with the expected stoichiometry, and reflecting the increase in the near-surface strontium content by ~50%, and again confirming that the (111) surfaces have the least strontium in the near-surface region. While we observe a change in

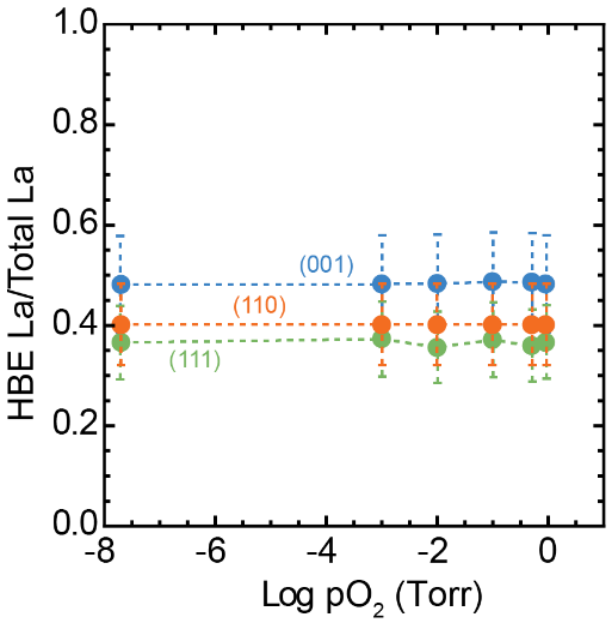

Supplementary Figure 14 | Pressure dependence of La *4d* components. . (Unlike the "surface" strontium concentration, which increases with increasing p_{O_2} at elevated temperatures, the relative contributions of the LBE and HBE components of the La *4d* excitation does not change over the course of the measurement.

the relative contributions of the LBE and HBE doublets for the strontium 3*d* over the course of the measurement, we observe no change in the relative contributions from LBE and HBE doubles for the lanthanum 4*d* excitation, which maintains a constant ratio for the duration of the measurements, indicating no change in surface lanthanum concentration and supporting the use of lanthanum as an internal standard for binding-energy calibration (Supplementary Fig. 14). Finally, the binding energy of the "surface" component of strontium is not the same for all three surface orientations, indicating the bonding environment of surface-terminated strontium is distinct on the different surfaces (Supplementary Fig. 15); however, no shift in these binding energies was observed with increasing p_{O_2}.

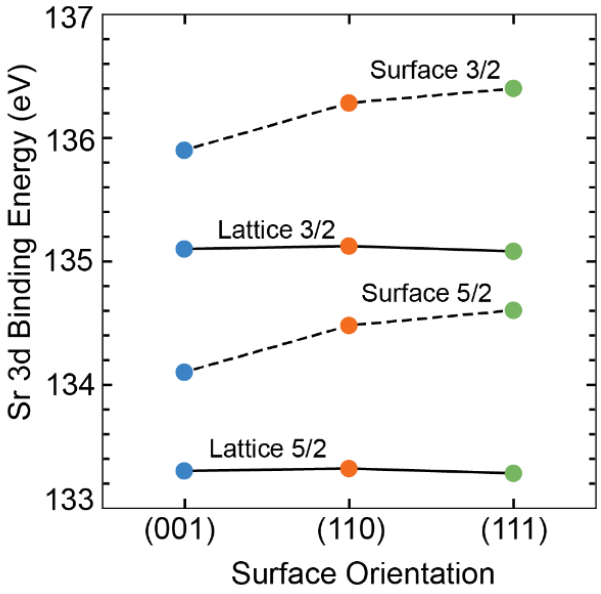

Supplementary Figure 15 | Binding energy evolution with surface orientation. The binding energies of the strontium 3*d* 3/2 and 5/2 excitations are compared across the three surface variants. No change is observed for the "lattice" component, as is expected for the three surface variants which have the same bulk chemistry. The "surface" components have binding energies differing by ~0.5 eV showing that (111) surface strontium have larger effective positive charge than those on the (110) or (001) surfaces.

References

1 J. Karthik, A. R. Damodaran and L. W. Martin, *Advanced Materials*, 2012, **24**, 1610–1615.

2 H. Téllez, J. Druce, Y.-W. Ju, J. Kilner and T. Ishihara, *Int J Hydrogen Energ*, 2014, **39**, 20856–20863.

3 J. Druce, T. Ishihara and J. Kilner, *Solid State Ionics*, 2014, **262**, 893–896.

4 J. Druce, H. Téllez, M. Burriel, M. D. Sharp, L. J. Fawcett, S. N. Cook, D. S. McPhail, T. Ishihara, H. H. Brongersma and J. A. Kilner, *Energy Environ Sci*, 2014, **7**, 3593–3599.

5 J. Fleig, F. S. Baumann, V. Brichzin, H. -R. Kim, J. Jamnik, G. Cristiani, H. -U. Habermeier and J. Maier, *Fuel Cells*, 2006, **6**, 284–292.

6 J. Fleig, H.-R. Kim, J. Jamnik and J. Maier, *Fuel Cells*, 2008, **8**, 330–337.

7 F. S. Baumann, J. Fleig, H.-U. Habermeier and J. Maier, *Solid State Ionics*, 2006, **177**, 1071–1081.

8 J. P. H. Li, X. Zhou, Y. Pang, L. Zhu, E. I. Vovk, L. Cong, A. P. van Bavel, S. Li and Y. Yang, *Phys Chem Chem Phys*, 2019, **21**, 22351–22358.

9 C. J. Powell and A. Jablonksi, *NIST Electron Inelastic-Mean-Free-Path Database - Version 1.2*, National Institute of Standards and Technology, Gaithersburg, MD, 2010.

10 E. J. Crumlin, E. Mutoro, W. T. Hong, M. D. Biegalski, H. M. Christen, Z. Liu, H. Bluhm and Y. Shao-Horn, *J Phys Chem C*, 2013, **117**, 16087–16094.

11 E. J. Crumlin, E. Mutoro, Z. Liu, M. E. Grass, M. D. Biegalski, Y.-L. Lee, D. Morgan, H. M. Christen, H. Bluhm and Y. Shao-Horn, *Energ Environ Sci*, 2012, **5**, 6081–6088.

12 S. Nemšák, G. Conti, G. K. Palsson, C. Conlon, S. Cho, J. E. Rault, J. Avila, M.-C. Asensio, C. A. Jackson, P. Moetakef, A. Janotti, L. Bjaalie, B. Himmetoglu, C. G. V. de Walle, L. Balents, C. M. Schneider, S. Stemmer and C. S. Fadley, *Appl Phys Lett*, 2015, **107**, 231602.

13 Z. Cai, M. Kubicek, J. Fleig and B. Yildiz, *Chem Mater*, 2012, **24**, 1116–1127.

14 A. K. Opitz, C. Rameshan, M. Kubicek, G. M. Rupp, A. Nenning, T. Götsch, R. Blume, M. Hävecker, A. Knop-Gericke, G. Rupprechter, B. Klötzer and J. Fleig, *Top Catal*, 2018, **61**, 2129–2141.

15 M. F. Sunding, K. Hadidi, S. Diplas, O. M. Løvvik, T. E. Norby and A. E. Gunnæs, *J Electron Spectrosc*, 2011, **184**, 399–409.

16 A. P. Grosvenor, B. A. Kobe, M. C. Biesinger and N. S. McIntyre, *Surf Interface Anal*, 2004, **36**, 1564–1574.

17 M. C. Biesinger, B. P. Payne, A. P. Grosvenor, L. W. M. Lau, A. R. Gerson and R. St. C. Smart, *Appl Surf Sci*, 2011, **257**, 2717–2730.